Volume 16
Number 13
7 July 2025
Pages 5191-5654

Food & Function

Linking the chemistry and physics of food with health and nutrition

rsc.li/food-function

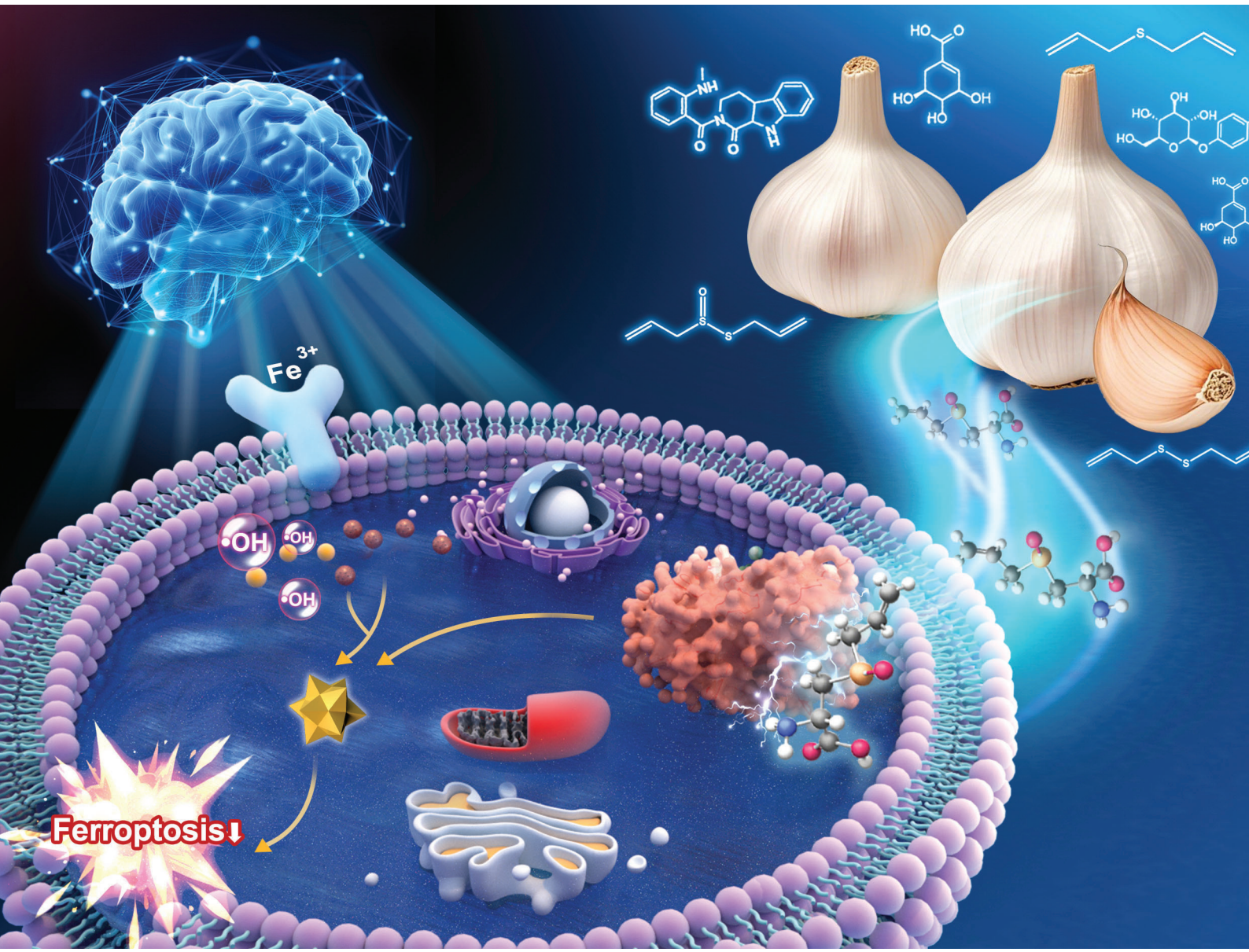

ISSN 2042-650X

ROYAL SOCIETY OF CHEMISTRY

PAPER

Junjun Meng, Chengquan Wen *et al.*
Alliin from garlic as a neuroprotective agent attenuates ferroptosis *in vitro* and *in vivo via* inhibiting ALOX15

Food & Function

ROYAL SOCIETY OF CHEMISTRY

PAPER

View Article Online
View Journal | View Issue

Cite this: *Food Funct.*, 2025, **16**, 5278

Alliin from garlic as a neuroprotective agent attenuates ferroptosis *in vitro* and *in vivo via* inhibiting ALOX15†

Junjun Meng,[a,b] Chengquan Wen,[c] Yang Lu,[d] Xiaofan Fan,[b] Ruili Dang,[a,b] Jianfeng Chu,[e] Pei Jiang, *[a,b] Wenxiu Han*[a,b] and Lei Feng *[f]

Alliin, a precursor active compound of sulfur-containing organic compounds such as allicin in garlic, is recognized as an important bioactive substance in garlic. Allicin has been shown to have significant neuroprotective effects and promote functional recovery in intracerebral hemorrhage (ICH). As a precursor of many active compounds, alliin may have broader therapeutic effects. Therefore, the aim of this study was to investigate the molecular mechanisms underlying the neuroprotective effects of alliin. In this study, we found that alliin inhibits ferroptosis, thereby exerting neuroprotective effects in ICH. However, the neuroprotective effects of alliin and its pharmacological mechanisms in ferroptosis have not been fully explored. The results showed that alliin significantly inhibited erastin-induced ferroptosis in HT22 cells and suppressed ferroptosis in the brain tissue of collagenase-induced ICH mice, alleviating neurological dysfunction and pathological damage. Mechanistically, alliin downregulated the expression of 15-lipoxygenase (ALOX15), which inhibits phospholipid peroxidation and ferroptosis. Moreover, gene knockout of ALOX15 produced effects similar to those of alliin, and comparable results were obtained using the ferroptosis inhibitor ferrostatin-1. This study is the first to demonstrate that alliin regulates ferroptosis both *in vitro* and *in vivo*. In conclusion, our study highlights ALOX15 as a critical factor in ferroptosis associated with ICH, and shows that alliin exerts neuroprotective effects by inhibiting ALOX15-dependent ferroptosis.

Received 24th January 2025,
Accepted 4th May 2025

DOI: 10.1039/d5fo00425j

rsc.li/food-function

1. Introduction

Garlic is an ancient medicinal and culinary plant that contains a variety of bioactive compounds, including almost all essential amino acids required by the human body. Garlic has anti-inflammatory, antibacterial, anticancer, and cancer-preventive properties, earning it the reputation of a "natural antibiotic".[1] It also possesses multiple neuroprotective activities.[2] Studies have shown that the main active component of garlic, allicin, reduces brain injury after intracerebral hemorrhage (ICH) by inhibiting apoptosis of perilesional cells and protecting the blood–brain barrier permeability, thereby improving the prognosis of ICH patients.[3] At the same time, allicin can alleviate early brain damage by inhibiting oxidative stress, inflammation, and brain edema, and by protecting blood–brain barrier function, thereby improving neurological function and exerting neuroprotective effects in brain injury.[2] Garlic and its extracts can protect neurons from ischemic brain injury, protect neurons in traumatic brain injury, and improve cognitive function in Alzheimer's disease,[4] with increasing attention to its neuroactive properties. The above studies indicate that garlic, as a characteristic agricultural product, possesses multiple neuroprotective activities.

Alliin is the primary active component among the organosulfur compounds found in garlic and serves as a precursor to allicin.[5] When raw garlic bulbs are crushed, cut, or ground, the vacuolar enzyme alliinase is released into the cytoplasm, catalyzing the conversion of alliin into diallyl thiosulfinate (allicin) (Fig. S1†).[6] Previous studies have shown that allicin and garlic extracts protect neural cells from ischemic brain injury,[7] traumatic brain injury.[8] They also safeguard neural cells from ischemic brain damage,[9] and allicin specifically improves neurological function and exerts protective effects on brain tissue following intracerebral hemorrhage (ICH).[3] Furthermore, allicin has been found to alleviate neurological

[a]*Translational Pharmaceutical Laboratory, Jining NO.1 People's Hospital, Shandong First Medical University, Jiankang Road, Jining 272000, China*
[b]*Shandong Provincial Key Medical and Health Laboratory of Neuroinjury and Repair, Jining NO.1 People's Hospital, Jining, 272000, China*
[c]*Department of Pharmacy, Qingdao Eighth People's Hospital, China*
[d]*Clinical College of Jining Medical University, China*
[e]*Department of Neurology, Jining No. 1 People's Hospital, Jining, China*
[f]*Department of Neurosurgery, Jining NO.1 People's Hospital, Jining, China. E-mail: flneuro@163.com; Fax: +86 537 2106208; Tel: +86 537 2106208*

† Electronic supplementary information (ESI) available. See DOI: https://doi.org/10.1039/d5fo00425j

dysfunction by inhibiting oxidative stress, suppressing inflammatory responses, reducing brain edema and blood–brain barrier (BBB) dysfunction, and decreasing apoptosis, thereby mitigating early brain injury and exerting neuroprotective effects.[9] Given these findings, we hypothesized that alliin, as the active precursor of allicin, may also possess significant neuroprotective activity. However, research on the neuroprotective effects of alliin has not yet been reported.

Ferroptosis, a form of iron-dependent non-apoptotic cell death, is characterized by biochemical features such as glutathione antioxidant dysfunction, depletion of glutathione peroxidase 4 (GPX4), lipid peroxide accumulation, and mitochondrial membrane shrinkage.[10] Following ICH, ferroptosis leads to the accumulation of lipid peroxides, which overwhelm cellular antioxidant defenses, resulting in the buildup of cytotoxic compounds, protein degradation, lipid damage, and neuronal death. Iron, a primary degradation product of hemoglobin breakdown, contributes to secondary brain injury after ICH by fostering the generation of free radicals and eliciting inflammatory reactions.[11] Iron toxicity primarily operates through the Fenton reaction, where iron generates abundant hydroxyl radicals, exacerbating tissue oxidation and causing neuronal cell damage.[12] This process plays a critical role in ICH pathogenesis.[13] The occurrence of ferroptosis after ICH exacerbates brain tissue damage and hinders the recovery of neurological function. Therefore, inhibiting ferroptosis can significantly prevent brain tissue damage and neurological dysfunction caused by intracerebral hemorrhage.

This study aims to elucidate the effects of alliin on ferroptosis and its underlying mechanisms, its protective effects on neural cells, and its neuroprotective role through the inhibition of ferroptosis following intracerebral hemorrhage. Therefore, in this study, we used network pharmacology methods to discover that the components in garlic can exert neuroprotective effects on ICH through the ferroptosis pathway. Through *in vitro* and *in vivo* experiments, combined with transcriptomics and metabolomics, we verified the effect of alliin attenuates neuronal injury by inhibiting ALOX15-dependent ferroptosis in erastin-induced HT22 cells and collagen-induced intracerebral hemorrhage. Thus, protects neural cells, alleviates neuronal injury, and promotes the recovery of neurological function.

2. Materials and methods

2.1. Main reagents

Alliin (No. A800878), Dimethyl sulfoxide (No. D8371), Ferrostatin-1 (Fer-1, No. HY-100579), Erastin (No. HY-15763), Type IV collagenase (No. C5138-100mg), 3-(4,5)-dimethylthiahiazo (-z-y1)-3,5-di-phenytetrazoliumromide (MTT, No. BS186-1g), JC-1 (No. 40706ES60), BODIPY™ 581/591 C11 (No. D3861), FerroOrange Cell Ferrous Ion Fluorescence Probe (No. 40706ES60), Lipid Peroxidation malondialdehyde Assay Kit (Nanjing Jiancheng Bioengineering Institute, No. A003-1-2), Glutathione Peroxidase (GSH-PX) assay kit (Nanjing Jiancheng Bioengineering Institute, No. A005-1-2), Lipid peroxidation assay kit (No. CB12932-Mu), Superoxide Dismutase (SOD) assay kit (Nanjing Jiancheng Bioengineering Institute, No. A001-3-2). ALOX15, GPX4, Zonula Occludens-1, Occludin, GAPDH, and NeuN (Abcam, USA). Alexa Fluor 488-labeled Goat Anti-Rabbit IgG(H + L) (No. A0423).

2.2. Network pharmacology prediction

The candidate targets of garlic were collected from three databases: SymMap (**https://symmap/org/**), the Traditional Chinese Medicine System Pharmacology (TCMSP) database and the Encyclopedia of Traditional Chinese Medicine (ETCM, **https://www.nrc.ac.cn:9090/ETCM/**) database. ICH-associated targets were collected from GenCards (**https://www.genecards.org/**). Through a process of cross-referencing the targets associated with garlic and ICH, potential active targets of garlic in the treatment of ICH were identified. Subsequently, compound-target and compound-target-pathway networks were constructed using Cytoscape 3.8.2. The overlapping targets were then subjected to Gene Ontology (GO) and Kyoto Encyclopedia of Genes and Genomes (KEGG) enrichment analysis through the DAVID Bioinformatics Resources 6.8 (**https://david.ncifcrf.gov/**), and Metascape database (**https://metascape.org/**). The top 15 GO and top 20 KEGG terms resulting from these analyses were selected for further detailed investigation. The bioinformatics online analysis platform (**https://www.bioinformatics.com.cn/**) was used to visualize the enrichment analysis results.

2.3. Molecular docking

Molecular docking analyses were conducted to investigate the binding affinities and interactions between active constituents and their potential targets. The 3D structure of alliin was retrieved from the PubChem database (CID: 87310). Energy minimization of the alliin structure was performed using ChemDraw 3D, and the resulting energy-minimized conformation was utilized for subsequent molecular docking simulations. The 3D structure of ALOX15 (PDB ID: 1LOX) was obtained from the Protein Data Bank (PDB). The protein structure was processed by removing water molecules and adding hydrogen atoms using Autodock Tools. Subsequently, the grid box position and size were set in blind docking mode to obtain more accurate binding sites. Molecular docking was performed using Autodock Vina 1.2.2. Binding energy was utilized to assess the binding interactions between ligands and receptor proteins. Discovery software was used to visualize receptor–ligand interactions.

2.4. *In vitro* study of alliin in ferroptosis

2.4.1. Cell culture and viability. HT22 cells were cultured using a DMEM medium containing 10% fetal bovine serum (FBS, A31608-02) at 37 °C with 5% CO_2. The culture medium also included 100 U ml^{-1} penicillin and 100 μg ml^{-1} streptomycin. 2.5% trypsin was used to dissociate cells when growth reached 90–95% efficiency. To explore the effect of alliin on ferroptosis induced by erastin, cells were treated with different

concentrations of alliin (0, 100, 200, 400, 600 μM) in the presence of erastin (1 μM) for another 24 h. Fer-1 (5 μM) was used as a positive control. MTT was used to assess the cell viability rates.

All experimental groups (including different concentration alliin treatment groups) all maintained the same final volume (such as 96-well plate 200 μl per well, 24 and 12-well plate 1 ml per well, 6-well plate 2 ml per well culture medium), through adjusting stock solution concentration to achieve target working concentration (100–600 μM).

2.4.2. Effect of ferroptosis inhibition in HT22 cells. HT22 cells were seeded at a density of 1×10^6 cells per well in 6-well plates and treated with erastin, alliin, and Fer-1 as mentioned above. JC-1, 2,7-Dichlorofuorescin diacetate (DCFH-DA, No. 50101ES01) and C11 BODIPY 581/591 were added to the wells. The cells were incubated for 20 minutes at 37 °C in the dark. Following incubation, the cells were washed twice with PBS, and a fluorescent microscope was used to observe them. The JC-1 monomer-to-polymer ratio was calculated to assess changes in mitochondrial membrane potential. Lipid peroxidation was quantified by calculating the ratio of the oxidized form of the dye to its normal form. FerroOrange was used to visualize intracellular Fe^{2+}. Fluorescence digital microscopy was used to measure fluorescence.

2.4.3. TEM translocation assays. HT22 cells (1 mm × 1 mm × 1 mm) were fixed in 2.5% glutaraldehyde and post-fixed in 1% osmium tetroxide for 2 hours. Gradient dehydration was performed with ethanol concentrations of 30%, 50%, 70%, 80%, 90%, and 100%. After drying, the cells were sputter-coated with gold, and mitochondrial ultrastructural images were captured using a transmission electron microscope (HT7700, Hitachi).

2.4.4. Gene silencing and efficiency assessment. The Mouse Alox15 gene was knocked out in HT22 hippocampal neuronal cells using CRISPR/Cas9 gene editing technology mediated by electroporation. After electroporation, single clones were selected and validated by PCR and sequencing, successfully obtaining homozygous Mouse Alox15 knockout cells.

2.5. *In vivo* study of alliin in ICH

2.5.1. Animals and drug administration. Wild-type male C57BL/6J mice (6–8 weeks old, 20–25 g) were purchased from Jinan Pengyue Experimental Animal Breeding Co., LTD (Jinan, Shandong, China). The study protocol was approved by the Ethics Committee of Jining NO.1 people's hospital (protocol number: JNRM2023DW009). A total of 80 mice were housed under a 12-hour light/dark cycle with 55–60% humidity and a constant temperature of 22 °C. After one week of adaptive feeding, the mice were randomly divided into three groups, control group (n = 26), ICH group (n = 28), alliin group (n = 26). Upon completion of the study period, all mice were euthanized and dissected under anesthesia following an overnight fast (12 h).

2.5.2. Alliin administration method. The pharmacokinetics and chemical properties of alliin were assessed using SwissADME, an online tool for evaluating drug-like properties. The BOILED egg plot was employed to predict gastrointestinal absorption and brain permeability.[14] Due to poor oral absorption from first-pass metabolism and limited blood–brain barrier penetration, tail vein injection was selected to ensure effective drug delivery and maximize therapeutic efficacy. Based on previous research demonstrating that 50 mg kg^{-1} allicin exerts neuroprotective effects in ICH models.[15] The same dosage of 50 mg kg^{-1} alliin was administered *via* tail vein injection in this study.

2.5.3. ICH Model. The ICH model was established by basal ganglia injection of collagenase as described.[16] Mice were anesthetized with 2% pentobarbital sodium (25 mg kg^{-1}) administered intraperitoneally. The mice were placed prone in stereotaxic frames (ZS-FD/S, China) to maintain stability during the procedure. Dental drills were used to drill a burr hole (1 mm deep, 2.0 mm on the right side of the bregma, 3.5 mm below the surface of the skull). ICH injury was induced by injecting type IV collagenase (0.1 U) dissolved in 1 μl saline in the hole at 0.2 μl min^{-1}. Drilling was carried out at a rate of 1 mm min^{-1} for 10 min to avoid reflux.

2.5.4. Behavioral assessment and animal weight. Prior to experimentation, animals should be gently manipulated to induce muscle relaxation and minimize resistance reactions. Subsequently, they should be positioned on the edge of a table. Upon contact of the whiskers of mice with the tabletop, healthy animals promptly place their ipsilateral forelimbs on the surface. The success rate of this forelimb placement task can be measured as the percentage of correct responses in 10 trials, typically requiring 5 minutes to complete. This assessment should be conducted within 1–3 days following induction of ICH.

2.5.5. Forelimb placing test. The forelimb placing test, also known as the whisker forelimb placing test, is conducted by holding the skin of the mouse's neck with one hand while gently pulling its tail with the other hand to extend the body. One side of the mouse's whiskers is slowly brought close to the edge of the table. When the whiskers touch the table edge, the normal response is for the corresponding forelimb to be placed at the edge of the table. However, the hemorrhagic stroke model group loses this reflex. In the experiment, each mouse is tested 10 times on each side, and the number of correct placements of the forelimb at the table corner following whisker contact is recorded. Prior to the formal experiment, the test animals are moved up and down several times with gentle handling to relax their muscles and reduce resistance.

2.5.6. Basso mouse scale (BMS). This open-field locomotor scoring system ranges from 0 to 9 points. Scoring criteria are as follows: 0 points-no ankle movement; 1 point-slight ankle movement; 2 points-extensive ankle movement; 3 points-plantar placement with or without weight support; 4 points-occasional plantar stepping; 5 points-frequent or consistent plantar stepping with no coordination; 6 points-frequent or consistent plantar stepping with some coordination, paws parallel at initial contact; 7 points-frequent or consistent plantar

stepping, mostly coordinated, paws parallel at initial contact and rotated at lift-off; 8 points-frequent or consistent plantar stepping, mostly coordinated, paws parallel at initial contact and lift-off, with mild trunk instability; 9 points-frequent or consistent plantar stepping, mostly coordinated, paws parallel at initial contact and lift-off, with normal trunk stability and the tail always elevated.

2.5.7. Morris water maze test (MWM). During the training in the water maze, the platform should be located in the center of the pool, 1 cm below the water surface, so that the animals are aware of its presence. Each animal will undergo three consecutive trials. First, the animal is placed on the platform for 20 seconds. The water maze has four starting positions: east, south, west, and north. The animal is placed in one of these positions. To place the animal in the water, support it with your hand and gently submerge its tail first. Avoid allowing the animal to enter the water headfirst to prevent causing stress. Allow the animal to swim/search for the platform, with a maximum time limit of 60 seconds. Initially, the animal may swim along the edge of the pool, searching for an exit. Eventually, the animal will learn to find the platform and climb onto it. Once the rodent reaches the platform, stop the timer and record the time. If it cannot find the platform within 60 seconds, record the trial time as one minute. If the animal fails to reach the platform, do not pick it up. You can use a glass or plastic rod to guide the animal to the platform, allowing it to rest on the platform for 15 seconds. Before the experimental trials in the water maze begin, fill the pool with tap water and heat it, setting the platform 1 cm below the water surface. Use non-toxic white temporary paint to make the water opaque. Facing the pool wall, the handler will place the animal in the water and then step back to a designated position to observe the animal completing the maze task. Analyze the animal until it reaches the platform and record the time taken.

2.5.8. Rotarod test. Mice are placed on the rotating rod in the compartment, which spins for 5 minutes to allow the mice to adapt to the new environment and mode of movement. After testing every five mice, the testing compartment is wiped with 75% alcohol to avoid interference from odors. During the testing phase, the procedure is the same as during the habituation phase. The rotarod motor function test is conducted at days 0, 9, and 16, where each mouse is placed on the rotarod, and the speed is adjusted to 40 rotations per minute. The time until the mouse falls off or undergoes passive continuous rotation for two complete turns is measured. Each experimental animal is tested three times with a 5-minute interval, and the average value is recorded as the result. The bottom of the box is fitted with a copper grid with 1 cm spacing, through which a 10 V current is applied to prevent the mice from jumping off the rotarod. During the experiment, the mice are placed on the rotating rod, and the time they remain on the rod is tested at 18 rotations per minute. The total distance traveled and average speed of the mice while on the rod are recorded. Each mouse is tested three times at each speed, and the average is taken. If a mouse remains on the rod for more than 120 seconds, it is recorded as 120 seconds. The time taken for the mouse to jump back onto the rod after receiving electrical stimulation upon falling off is also noted. If the mouse does not jump back onto the rod within 120 seconds, it is recorded as 120 seconds.

2.5.9. Beam walking test. The beam walking test is a popular method for analyzing mouse gait in environments that challenge their balance. The test is conducted over three consecutive days: two days of training and one day of testing. Performance on the beam is quantified by measuring the time it takes for the mouse to cross and the number of slips that occur during the process. A series of five narrow beams is used to assess their motor coordination and balance. A 1-meter long beam is positioned horizontally, 0.5 meters above the ground, with one end mounted on a narrow support and the other connected to a cage from which the mouse can escape. Animals undergo three training trials on the training beam with three different starting points: near the home cage, at the center of the beam, and at the brightly lit end. After training, the mice undergo five consecutive test trials, with one attempt on each beam. The difficulty increases with each attempt. The test trials are recorded and subsequently evaluated. Mice are made to cross a round wooden beam with a diameter of 1.5 cm and a length of 70 cm, elevated 30 cm off the ground. After crossing, they receive corresponding scores. The test is repeated three times, with scores determined based on walking distance and gait (0–4 points).

2.5.10. Brain water content measurement. 48 h after ICH, and the brains were extracted and divided into two parts: the right and left hemispheres. In order to determine the dry weight of each part, we weighed it immediately after it came out of the oven, using an electric analytic balance (AR224CN, China). Brain water content (%) = [(wet weight-dry weight)/wet weight] × 100%.[17]

2.6. Transcriptomics analysis in brain after ICH

Using a Novaseq 6000 platform, 150 bp paired-end reads were generated from the libraries. HTSeq-count4 was used to estimate FPKM3 and read counts for each gene. An analysis of PCA was conducted using R (v 3.2.0) to determine whether samples were biologically duplicated. *P*-values <0.05 and |log2 FC| > 1 was set as the threshold for significantly differential expression gene.

2.7. Metabolomics analysis

Brain samples from the control and ICH groups were selected for untargeted metabolomics analysis. The analytical instrument is a LC-MS system. Chromatographic column: ACQUITY UPLC HSS T3 (100 mm × 2.1 mm, 1.8 um), column temperature: 45 °C, mobile phase: water (containing 0.1% formic acid), acetonitrile, flow rate: 0.35 ml min^{-1}; injection volume: 3 μl. To visualize the difference between the two groups (control and ICH), PCA and PLS-DA scores were plotted. There was statistical significance assigned to metabolites with *p*-values <0.05 and |log2 FC| > 1.

2.8. Hematoxylin–eosin (HE) staining

After deeply anesthetizing the mice, transcardial perfusion was performed using 40 ml of cold phosphate-buffered saline (PBS). Brain tissue was then removed, fixed in 4% paraformaldehyde, and embedded in paraffin. HE staining was conducted on the deparaffinized brain tissue sections according to the manufacturer's instructions.

2.9. Immunofluorescence staining

The HT22 cells and brains were removed and preserved in 4% PFA solutions at 4 °C for 24–48 hours, and then soaked in 30% sucrose solutions for 72 hours to dehydrate completely. Next, the brain were sliced into 8 μm sections for immunofluorescence staining. Immufluorescence was performed on the slides by reheating for 30 minutes at room temperature, rinsing three times with PBS, then blocking for 60 minutes at room temperature with QuickBlotTM Blocking Buffer. After incubation with primary antibodies (12 h, 4 °C), anti-NeuN, anti-ALOX15 and anti-GPX4 were applied. Subsequently, the slides underwent a second rinsing process and were then exposed to fluorescence-conjugated secondary antibodies that corresponded to the primary antibodies for a duration of two hours at a temperature of 25 °C. The final step was to use a fluorescence microscope to take images (Olympus Co., Tokyo, Japan).

2.10. Measurement of MDA, SOD, LPO and GSH-Px

The MDA, SOD, LPO, GSH-Px content was measured according to the manufacturer's protocol.

2.11. Western blotting

According to the above description, HT22 cells and brain were treated. The total protein of the brain and whole cell was extracted using the whole-cell lysis assay (R0010) and the nuclear and cytoplasmic protein extraction kit (EX1580). The manufacturer's instructions were followed for the use of the bicinchoninic acid (BCA) protein quantitation assay (Omni-Easy, China, ZJ102). Following this, the slides were mounted using Fluoroshield Mounting Medium containing DAPI. The proteins were separated using 12% sodium dodecyl sulfate (SDS)-polyacrylamide gels and subsequently transferred onto PVDF membranes (Millipore, IPVH00010). TBST containing 0.01% Tween 20 was used to block the membranes, followed by primary antibodies against ALOX15, GPX4 and GAPDH (control) at room temperature for 1 h. TBST was used to wash the membranes three times for 10 minutes before incubating them with rabbit anti-goat antibody conjugated with horseradish peroxidase (HRP). A Tanon 4800 FluorChem® M MultiFluor system (Tanon) was used to detect the target protein bands after three TBST washes for 10 minutes. Image J was used to determine the density of the protein bands.

2.12. Statistical analysis

Data are expressed as mean ± standard deviation. Data analysis was performed using GraphPad Prism 8 (GraphPad, San Diego, CA, USA). One-way analysis of variance (ANOVA) was utilized, followed by Duncan's multiple-range test to evaluate differences among the groups. The data were analyzed by one-way ANOVA. A p-value less than 0.05 was considered significant.

3. Results

3.1. Network pharmacology analysis

A comprehensive search across the TCMSP, SymMap, and the ETCM databases revealed a total of 100 garlic ingredients, comprising 29 organic sulfides, 19 polyphenols, 16 amino acids and derivatives, 7 flavonoids, and 29 others. The neuroprotective capabilities of garlic extracts suggesting these ingredients may contribute to garlic's efficacy in ICH treatment.[18,19] Thus, despite some ingredients not meeting standard criteria for oral bioavailability[20] and drug-likeness,[21] they were included as active compounds. Based on our previous research on the nutritional components of different garlic varieties, we selected 71 candidate compounds and searched for their corresponding targets in databases, identifying a total of 340 potential targets (Table S1†).[22] Interactions between compounds and targets were established and visualized using Cytoscape 3.8.2 (Fig. 1A).

To identify potential targets associated with ICH, we searched four databases for relevant research reports, yielding a total of 6114 ICH-related targets. Subsequently, venn diagram analysis was employed to identify the intersection between garlic target genes and ICH target genes, revealing a total of 98 shared target genes (Fig. 1B). To explore the key biological processes influenced by garlic in ICH treatment, we performed GO functional enrichment analyses. The results unveiled that these 98 genes were enriched in 342 GO entries, encompassing 218 biological processes (BP), 45 cellular components, and 79 molecular functions (MF), the top 15 GO terms were depicted in Fig. 1C. The top 5 BP items highlighted that the associated targets primarily revolved around response to lipopolysaccharide, response to xenobiotic stimulus, response to amyloid-beta, positive regulation of cell population proliferation, chemical synaptic transmission. The top 5 CC items indicated that the related targets were predominantly located in neuron projection, plasma membrane, cytoplasm, membrane and cytosol. The top 5 MF items revealed that the potential targets were mainly associated with nuclear receptor activity, peptide hormone binding, protein homodimerization activity, protein lysine deacetylase activity, amyloid-beta binding. In addition, the significantly enriched MF also includes heme binding and iron ion binding. To investigate the prominent signaling pathways associated with key targets, we conducted KEGG enrichment analysis. The results unveiled 20 significantly enriched pathways ($P < 0.05$) (Fig. 1D), encompassing pathways such as ferroptosis, arachidonic acid metabolism, steroid hormone biosynthesis, and pathways linked to neurodegenerative diseases, among others. Notably, the predicted targets associated with the ferroptosis signaling

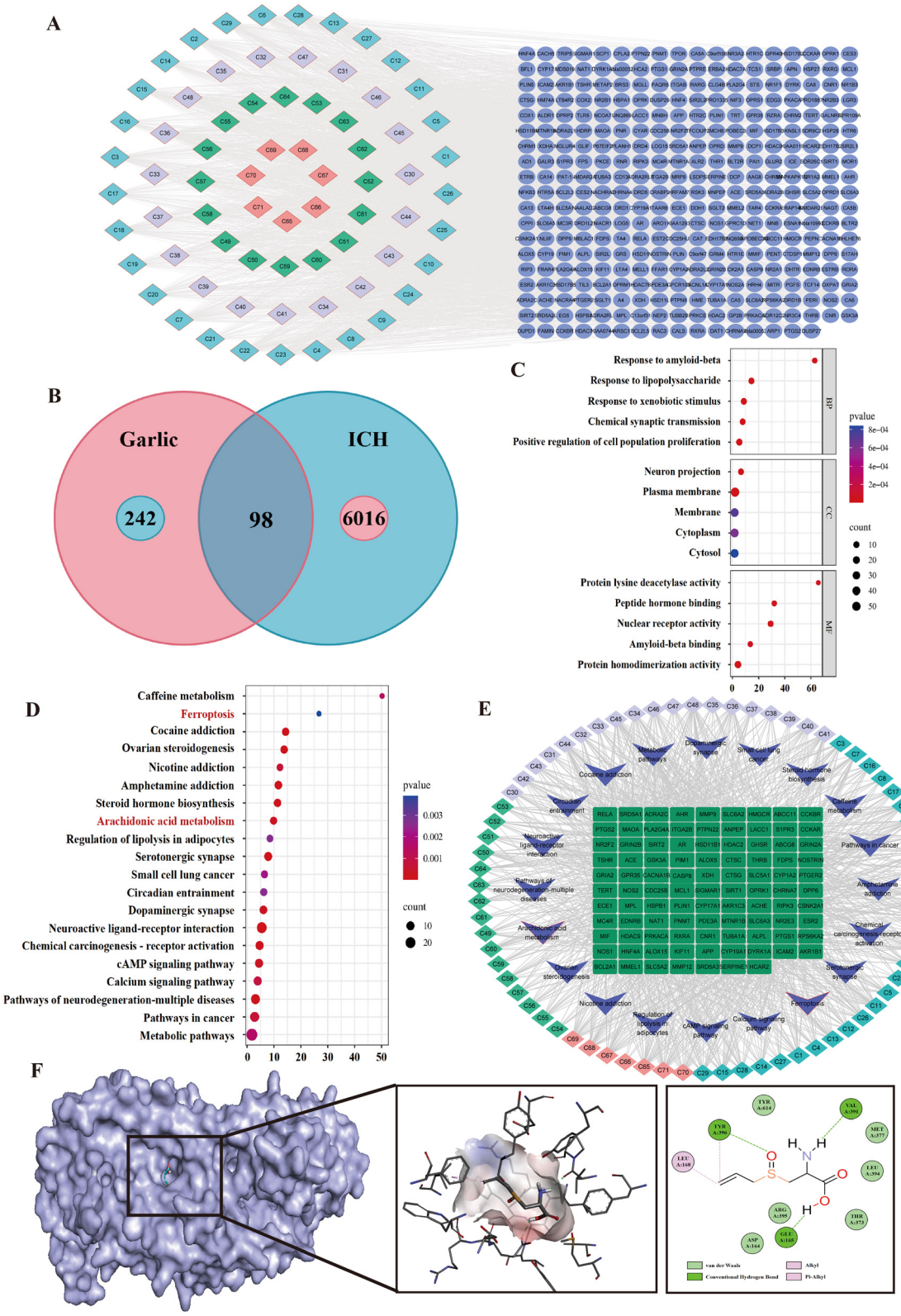

Fig. 1 Network pharmacology uncovers the mechanism of garlic for ICH. (A) Garlic component and potential targets network. (B) Venn diagram of targets shared by garlic and ICH. (C) GO-enrichment analysis of common targets. (D) KEGG pathway analyses of the hub genes. (E) Garlic component-target-ICH network. (F) Molecular docking analysis identifies potential binding regions between alliin and ALOX15.

pathway included APP, ALOX15, and PTGS2. The arachidonic acid metabolism is associated with ferroptosis, and the predicted targets associated with the arachidonic acid metabolism signaling pathway also included ALOX15. Subsequently, to elucidate the interconnections among active compounds, targets and ICH, we constructed a drug–target–disease network using Cytoscape 3.8.2 software (Fig. 1E). The results of network pharmacology preliminarily suggest that the active components in garlic can act on arachidonic acid metabolism and inhibit the occurrence of ferroptosis.

3.2. Molecular docking

To further explore the interactions between the five core components (allicin, DAS, DADS, DATS, and alliin) and the target ALOX15 in the ferroptosis pathway, and to elucidate a novel drug development strategy, we conducted additional molecular docking simulations (Fig. 1F). Through these simulations, we determined the binding affinity between the five compounds and the key target protein ALOX15 within the ferroptosis signaling pathway. The docking scores indicate that most of these compounds exhibit excellent binding activity (Table S2†). It can be concluded that alliin binds to ALOX15 transcriptional proteins with a lower energetic than other components, −5.0 kcal mol^{-1}. As a result of receptor–ligand docking, lower docking energy suggests higher protein–ligand binding affinity. The interaction between alliin and ALOX15 involves van der Waals forces with residues Tyr614, Met377, Leu394, Thr373, Arg395, and Asp164. Pi (π)-alkyl and alkyl interactions with Leu168 and Tyr396 residues further contribute to the stability of the alliin-ALOX15 complex. Additionally, alliin forms stable hydrogen bonds with Glu165, Val391, and Tyr396. A hydrogen bond is formed between the hydroxyl group of alliin and the carboxyl group of Glu 165, with a bond length of 2.8 Å. Another hydrogen bond is formed between the thioether group of alliin and the carbonyl group of Val 391, with a bond length of 3.0 Å. A third hydrogen bond is formed between the amino group of alliin and the hydroxyl group of Tyr 396, with a bond length of 2.9 Å (Fig. S2A†). Meanwhile, electrostatic interactions formed between alliin and nearby amino acid residues in the binding pocket further enhance binding stability (Fig. S2B and C†). Overall, the ligand molecule exhibits stable binding to the protein's active pocket, demonstrating complementary structural conformation and electrostatic distribution, while being stabilized by sufficient intermolecular interactions.

3.3. The changes of transcriptome in brain after ICH

Before conducting in-depth research on the effect of alliin on ferroptosis after ICH based on the ALOX15 target, we first conducted transcriptomic analysis on the brain tissue of ICH mice. The purpose was to confirm that ferroptosis occurs in mouse brain tissue after ICH, and the occurrence of ferroptosis is related to ALOX15.

Principal component analysis (PCA) revealed distinct separations among these groups (Fig. S3A†). There were 734 differentially expressed genes in ICH group compared to the control group (503 up-regulated and 231 down-regulated) as shown in Fig. 2A. The heatmap resulting was shown in Fig. 2B, this indicates significant changes in the genes of the brain tissue after ICH. GO function enrichment analysis of the upregulated genes (Fig. 2C) showed that compared to the control group, the differentially expressed genes in the ICH group were mainly enriched for arachidonic acid epoxygenase activity, iron ion binding, heme binding, and oxidoreductase activity. For cellular component, differential genes were mainly enriched for haptoglobin-hemoglobin complex, collagen-containing extracellular matrix, mitochondrial respiratory chain complex I, *etc*. According to various previous studies, arachidonic acid epoxygenase activity and iron ion could regulate ferroptosis.[23,24] Consistent with GO analysis results, KEGG pathway analysis showed that these upregulated genes were enriched in 20 signaling pathways, mainly included 8 metabolism pathways, 3 lipid metabolism pathways, include arachidonic acid metabolism, linoleic acid metabolism, oxidative phosphorylation, and steroid hormone biosynthesis, *etc.* (Fig. 2D). The targets associated with these pathways are shown in Fig. 2E. The top 20 reactome enrichment pathways were scavenging of heme from plasma, plasma lipoprotein assembly, remodeling, and clearance, plasma lipoprotein remodeling, plasma lipoprotein assembly, and metabolism, *etc.* (Fig. S3B†). The top 20 wikipathways enrichment were fatty acid omega-oxidation, iron homeostasis, oxidative phosphorylation, fibrin complement receptor 3 signaling pathway, adipogenesis genes, *etc.* (Fig. S3C†).

3.4. The changes of metabolisms in brain after ICH

Metabolomic analysis further indicated that ferroptosis occurred after ICH, leading to the accumulation of lipid peroxides. The changes in metabolites between the ICH and control groups were examined using an animal model. PCA showed that the ICH group was well separated from the control group (Fig. 3A). Based on $p < 0.05$ and $|\log_2 FC| > 1$ screening conditions, a total of 102 differential metabolites were identified. The categorization of these 102 metabolites is shown in Fig. 3B, lipids and lipid-like molecules account for 25.05%. This indicates that lipids has significantly changed after ICH. Among them, 30 metabolites were downregulated and 72 metabolites were upregulated (Fig. 3C). The upregulated metabolites in ICH group include PC, PE, DG, and other lipids (Fig. 3D). The KEGG analysis revealed that the metabolic pathways predominantly encompassed linoleic acid metabolism, α-linolenic acid metabolism, arachidonic acid metabolism, glycerophospholipid metabolism, and glycerolipid metabolism, *etc.* (Fig. 3E). The metabolomic data suggest that, following ICH, neurons undergo ferroptosis, resulting in cytoplasmic membrane disruption and lipid accumulation.

3.5. Alliin increased the cell viability in erastin-induced HT22 cells

In order to assess the inhibitory effects of alliin on ferroptosis following ICH, an *in vitro* ferroptosis model induced by erastin

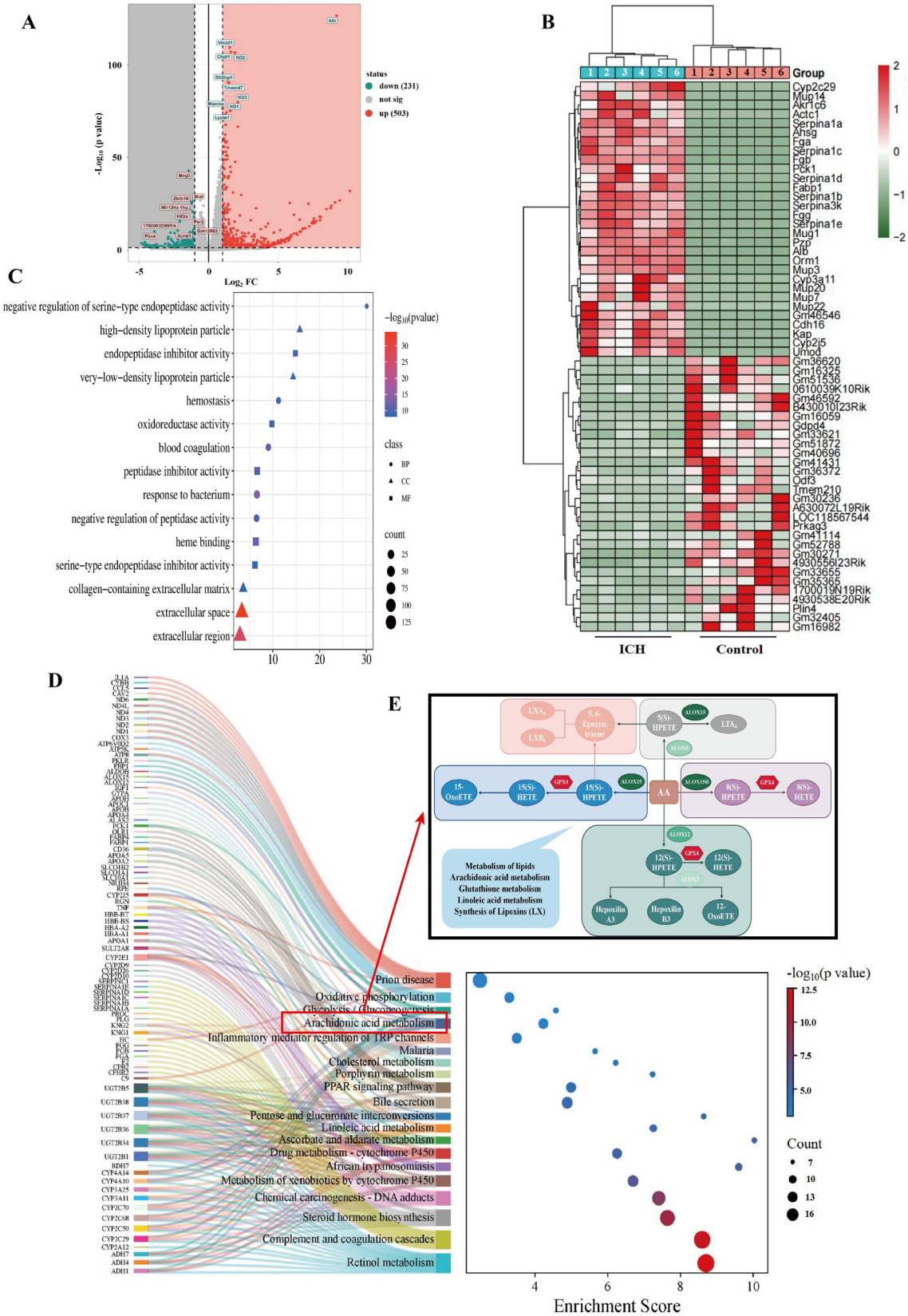

Fig. 2 Transcriptomic differences in the brain between control and ICH group. (A) Volcano plots of differential genes in the ICH *vs.* control group. (B) Heatmap of the differential genes. (C) GO analysis of the differential genes. (D) KEGG enrichment of the top 20 pathways. (E) Biosynthetic pathways for LXs production.

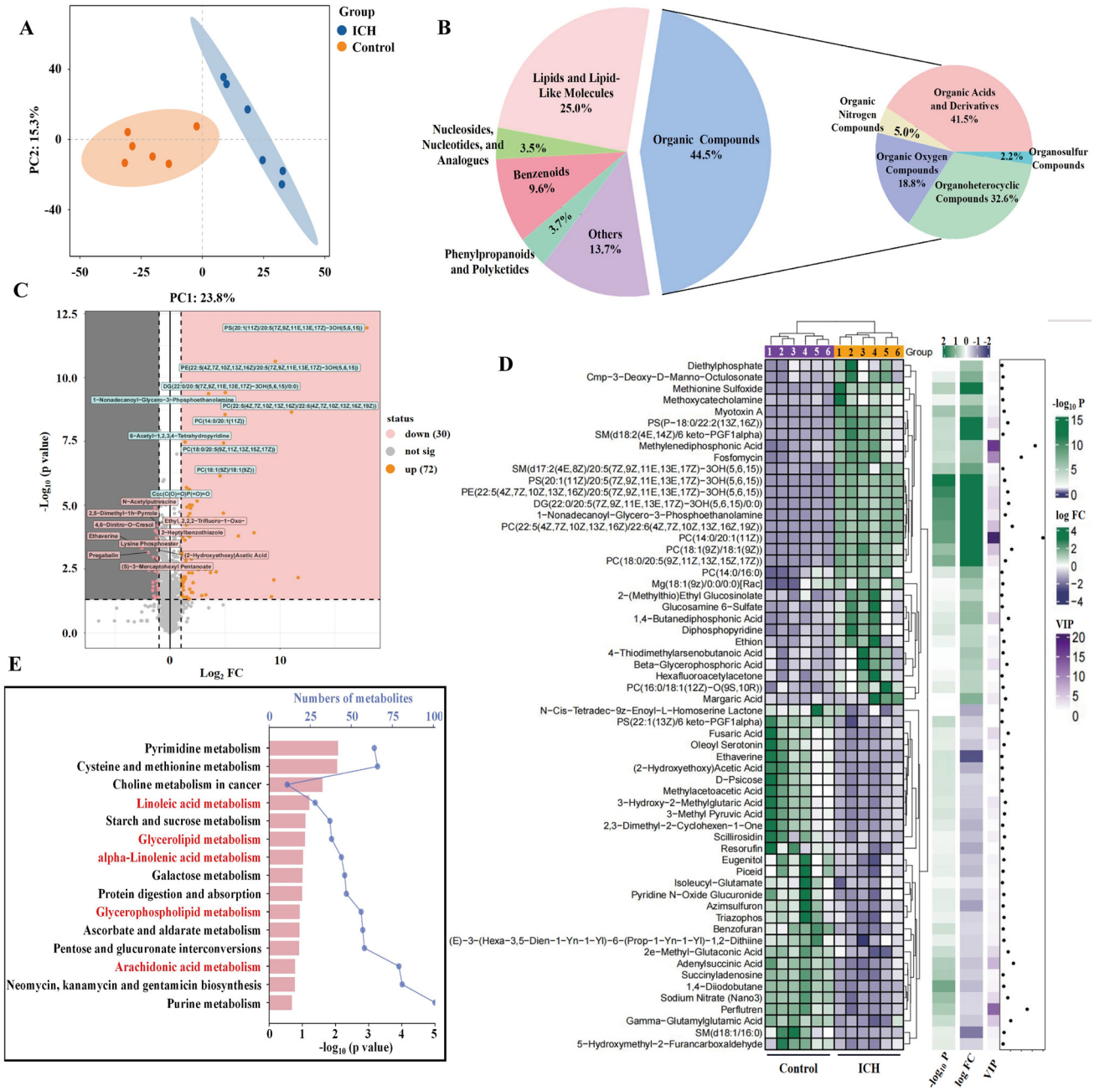

Fig. 3 Differential metabolites in the brain between control and ICH group. (A) PCA plot among the two groups. (B) Classification pie chart of differential metabolites. (C) Volcano plots of differential metabolites in the ICH *vs.* control group. (D) Heatmaps of the differential metabolites. (E) KEGG enrichment of the top 15 pathways.

was established (Fig. 4A and B). MTT assays were subsequently performed to assess the effect of alliin on erastin-induced cytotoxicity in HT22 cells. Due to the limited research on ALOX15 and the lack of specific inhibitors for ALOX15, we used the ferroptosis inhibitor Fer-1 as the positive control group in our experiment. Results indicated that erastin decreased HT22 cell viability, while alliin demonstrated a concentration-dependent enhancement of cell viability (100, 200, 400, 600 μM) (Fig. 4C).

3.6. Alliin suppressed ROS accumulation and increased the MMP in HT22 cells

Transmission electron microscopy[25] revealed alterations in mitochondrial ultrastructure. Following treatment with alliin and Fer-1, mitochondria exhibited regular morphology and reduced vacuolation. In contrast, the erastin group showed increased mitochondrial membrane density and a loss of mitochondrial cristae (Fig. 4D). These mitochondrial characteristics

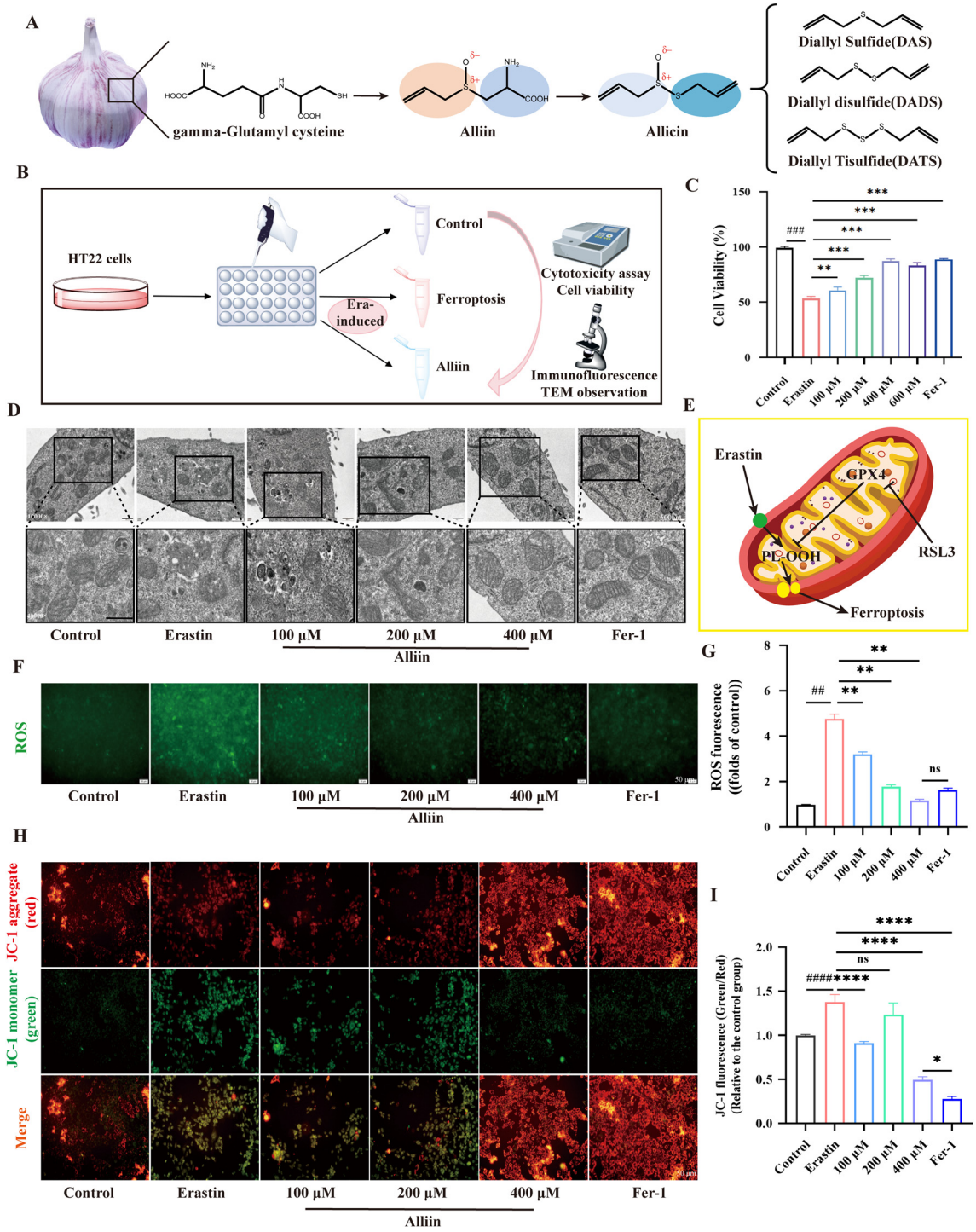

Fig. 4 Alliin increases the cell viability, decreased the levels of mitochondrial damage in erastin-injured HT22 cells. (A) The chemical structure of alliin in garlic. (B) Overall flow. (C) Effects of different concentrations alliin on the viability of erastin-injured HT22 cells. (D) Mitochondrial morphology was observed using TEM (Scale bar, 500 nm). (E) The relationship between ferroptosis, PUFAs and mitochondria. (F and G) Alliin decreased production of intracellular ROS (Scale bar, 50 um). (H and I) JC-1 staining indicated that alliin can increase the MMP of the HT22 cells (Scale bar, 50 um). $^{\#}$Compared with control group, *compared with erastin group, $^{*/\#}P < 0.05$, $^{**/\#\#}P < 0.01$, $^{***/\#\#\#}P < 0.001$, $^{****/\#\#\#\#}P < 0.0001$, "ns" means no significant difference ($P > 0.05$).

are closely associated with cellular ferroptosis (Fig. 4E). We conducted the DCFH-DA assay on HT22 cells to assess the effect of alliin in mitigating the excessive ROS produced by erastin-induced ferroptosis. The results showed minimal green fluorescence intensity in the control group, indicating the absence of ROS. However, a substantial increase in green fluo-

rescence was observed in the erastin-treated HT22 cells, attributable to oxidative stress induced by erastin. Treatment with alliin and Fer-1 significantly reduced the green fluorescence intensity, thereby rescuing neuronal cells from ferroptosis, demonstrating its potential to eliminate excessive ROS (Fig. 4F and G). We then questioned whether the mitochondrial fragmentation observed under erastin-induced ferroptosis could also extend to a decrease in mitochondrial membrane potential (MMP). To explore this, we employed JC-1 staining to detect both quantitative and qualitative changes in MMP. In this research, MMP was evaluated using JC-1 probe staining, with elevated MMP levels manifesting as red fluorescence due to JC-1 polymer aggregation. Conversely, decreased MMP levels were indicated by green fluorescence as JC-1 remained in its monomeric state. The results demonstrated that the alliin-treated group displayed significantly higher MMP levels compared to the erastin group, indicating that alliin helps preserve mitochondrial integrity (Fig. 4H and I).

3.7. Alliin decreased Fe^{2+} accumulation and oxidative damage in HT22 cells

The utilization of a FerroOrange probe, designed to selectively interact with Fe^{2+} within living cells, was employed to track the accumulation of Fe^{2+} in live cells. Results demonstrated that both alliin and Fer-1 were effective in reducing the cellular Fe^{2+} levels in comparison to those observed in the erastin-treated group (Fig. 5A and B). Fer-1 is a foundational research tool in ferroptosis studies, functioning by targeting lipid peroxidation, though its clinical translation is limited by stability issues. Experimental results demonstrate that alliin, a naturally derived compound with stable structure and low toxicity, can significantly inhibit Fe^{2+} accumulation during ferroptosis. The lipid-soluble ratiometric fluorescent indicator C11 BODIPY 581/591 demonstrates spectral shifts in its excitation and emission maxima from 581 to 500 nm and 591 to 510 nm, respectively. The lipid-soluble ratiometric fluorescent indicator C11 BODIPY 581/591 demonstrates spectral shifts in its excitation and emvely, following oxidation. This indicator has been utilized in various biochemical assays and live-cell investigations. In a study utilizing C11 BODIPY 581/591 to evaluate lipid peroxidation, lower levels of lipid peroxidation were observed in the alliin group compared to the erastin group (Fig. 5C and D).

3.8. Alliin affects ferroptosis through ALOX15 and GPX4 expression in erastin-injured HT22 cells

The study conducted cellular localization analysis of ALOX15 expression in HT22 cells through immunofluorescence staining. The findings revealed a significant decrease in cell count and an increase in ALOX15 expression in cells induced with erastin. Conversely, alliin was found to enhance cell survival and suppress ALOX15 expression in HT22 cells (Fig. 5E). The expression levels of ALOX15 and GPX4 were measured using western blot analysis. Our results indicate that in the alliin-treated group, ALOX15 expression was reduced compared to the erastin-treated group, while GPX4 expression was increased (Fig. 5F–H). The findings of our study indicate that alliin suppresses the generation of lipid peroxides associated with ferroptosis by downregulating the expression of ALOX15.

3.9. Alliin inhibits erastin-induced ferroptosis in HT22 cells through an ALOX15-dependent mechanism

To further confirm that the protective effect of alliin is related to ALOX15, the ALOX15 gene in HT22 hippocampal neuronal cells from mice was knocked out using CRISPR/Cas9 gene editing technology mediated by electroporation. Then we examined the expression of the ferroptosis-related regulatory factor GPX4 and found that ALOX15 knockout (Fig. 6A and B) reversed the erastin-induced downregulation of GPX4 and eliminated the regulatory effect of alliin (Fig. 6C and D). The immunofluorescence staining of cell localization results further confirmed this conclusion (Fig. 6E). Furthermore, ALOX15 knockout alleviated the accumulation of ROS (Fig. 6F and G), JC-1 (Fig. 6H and I), and Fe^{2+} (Fig. 6J and K). The above results indicate that the role of alliin in regulating ferroptosis in HT22 cells is related to ALOX15.

3.10. Transcriptome changes between alliin and ICH group

To further elucidate the impact of alliin on ferroptosis following ICH, specifically targeting ALOX15, we conducted transcriptomic analysis on the brain tissue of mice between alliin and ICH groups. PCA revealed distinct separations among these groups, indicating that the establishment of the model could impact the transcriptional profiles (Fig. 7A). There were 1843 differentially expressed genes in alliin group compared to the ICH group (301 up-regulated and 1542 down-regulated) as shown in Fig. 7B. The heatmap resulting from additional cluster analysis of ferroptosis-related genes was shown in Fig. 7C, this indicates significant changes in the genes of mouse brain tissue after alliin treatment. GO function enrichment analysis of downregulated genes (Fig. S4†) showed that compared to the ICH group, the differentially expressed genes in the alliin group were mainly enriched for hemoglobin complex, haptoglobin-hemoglobin complex, HFE-transferrin receptor complex, haptoglobin binding, peroxidase activity, hemoglobin alpha binding, related to the binding and transport proteins of Fe^{3+} on the membrane. Fig. 7D shows the top 20 enriched pathways of Reactome, such as heme signaling, synthesis of lipoxins (LX), synthesis of 12-eicosatetraenoic acid derivatives, *etc*. Fig. 7E shows the top 20 enriched pathways of Wikipathways, such as eicosanoid metabolism *via* lipoxygenases (LOX) and iron homeostasis, *etc*. The enriched pathways were analyzed in three databases, Fig. 7F shows some significantly enriched related pathways, such as arachidonic acid metabolism and Lipid and atherosclerosis, *etc*. The transcriptomic results once again confirmed that alliin can inhibit the occurrence of lipid peroxidation after ferroptosis in brain tissue after ICH.

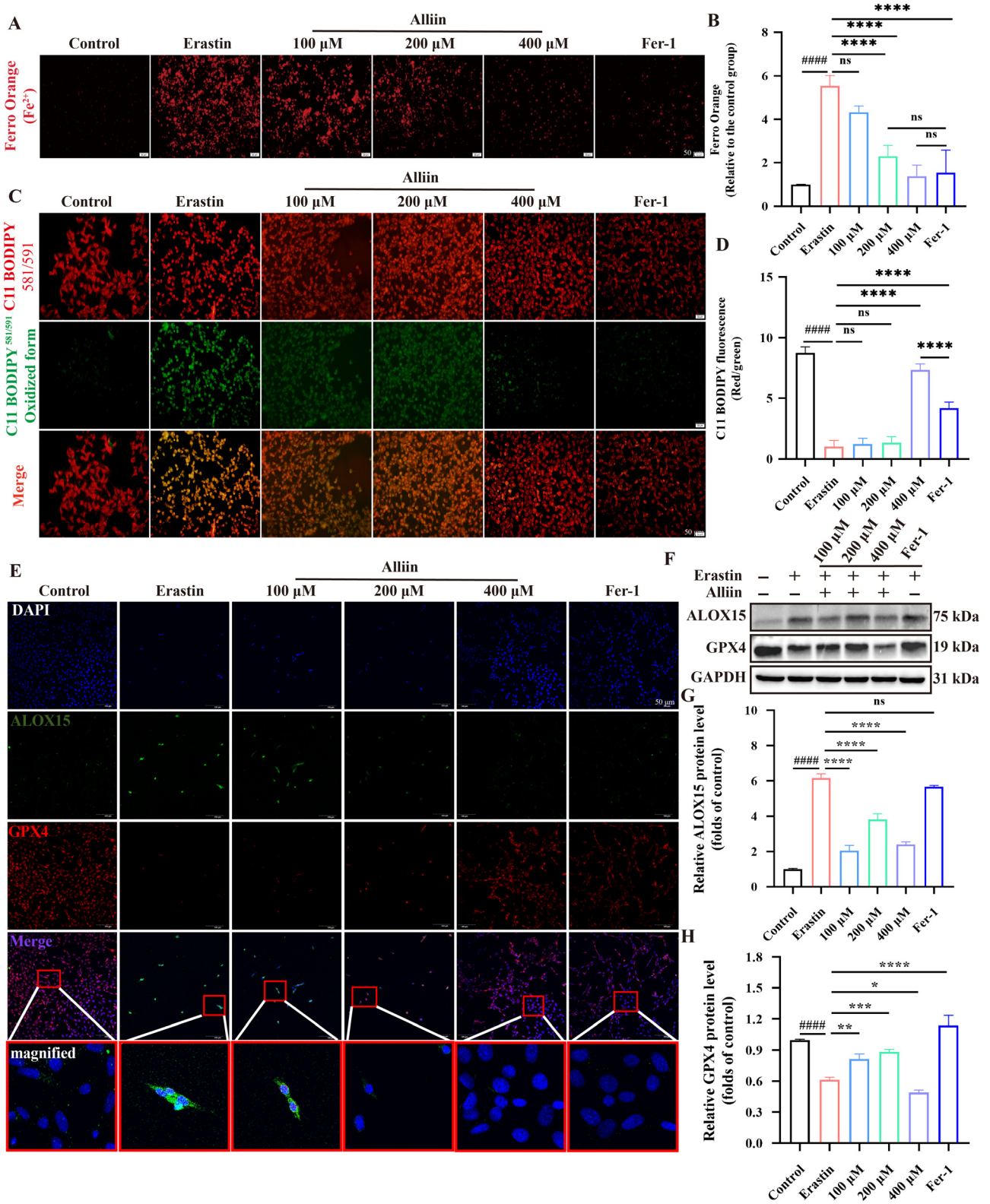

Fig. 5 Alliin decreased the accumulation of lipid peroxidation and influenced the expression of ALOX15 and GPX4. (A and B) Alliin and Fer-1 decreased the content of cell Fe^{2+}. (C and D) Alliin decreased the accumulation of lipid peroxidation. (E) Representative photographs of colocalization of ALOX15 in green and GPX4 (red) with HT22 cells. (F–H) The expression of ALOX15 in the alliin group was decreased while the GPX4 was increased compared with the erastin group. Scale bar 50 um, $^{\#}$compared with control group, *compared with erastin group, $^{*/\#}P < 0.05$, $^{**/\#\#}P < 0.01$, $^{***/\#\#\#}P < 0.001$, $^{****/\#\#\#\#}P < 0.0001$, "ns" means no significant difference ($P > 0.05$).

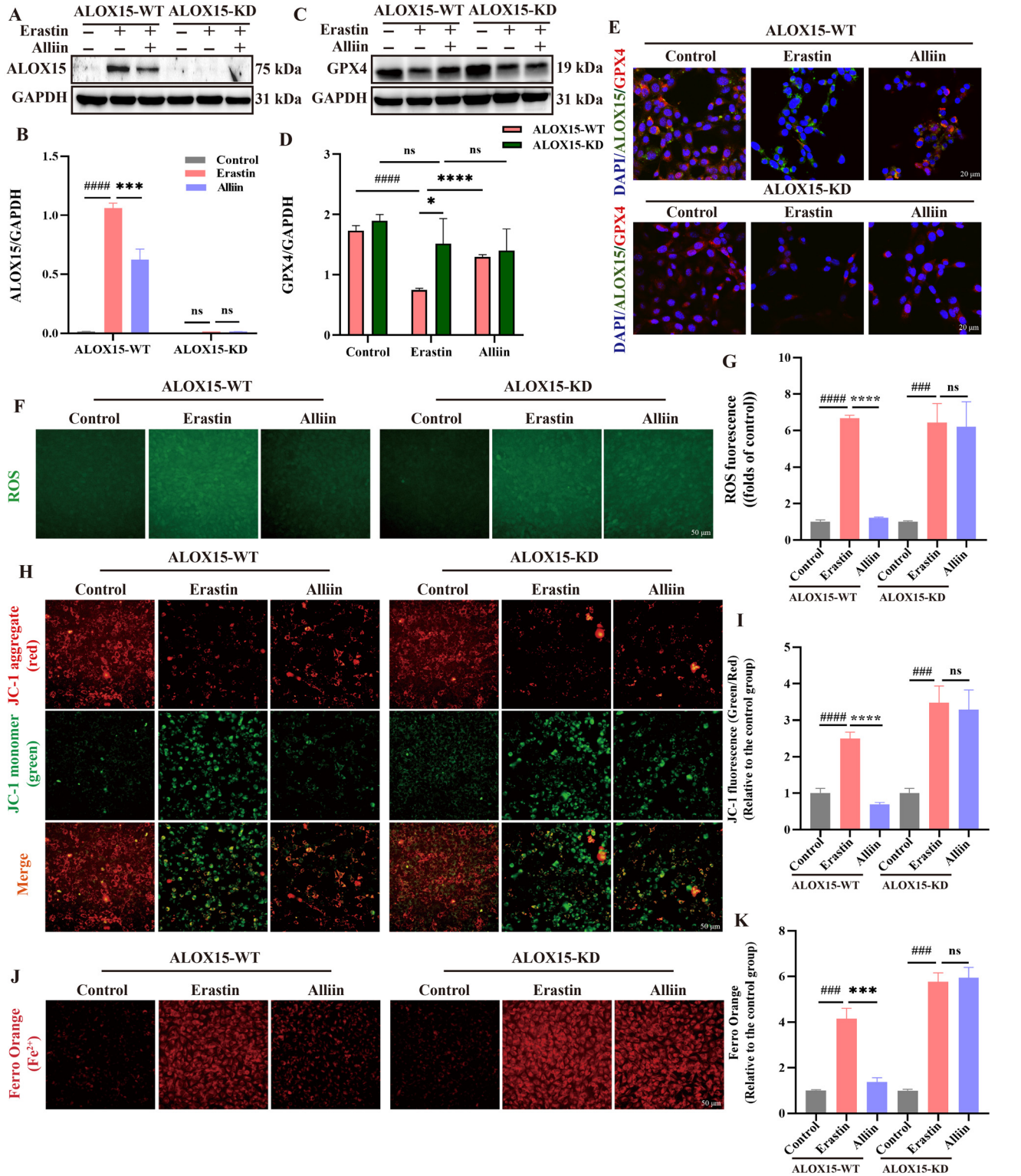

Fig. 6 In ALOX15-KD HT22 cells, alliin did not alleviate erastin-induced cell ferroptosis. (A–D) Western blot analysis of ALOX15 and GPX4. (E) Representative photographs of colocalization of ALOX15 in green and GPX4 (red) in ALOX15-KD HT22 cells. (F and G) Alliin did not decreased production of intracellular ROS. (H and I) JC-1 staining of the ALOX15-KD HT22 cells. (J and K) The content of Fe^{2+} in ALOX15-KD cells. Scale bar 50 um, #compared with control group, *compared with erastin group, $^{*/\#}P < 0.05$, $^{**/\#\#}P < 0.01$, $^{***/\#\#\#}P < 0.001$, $^{****/\#\#\#\#}P < 0.0001$, "ns" means no significant difference ($P > 0.05$).

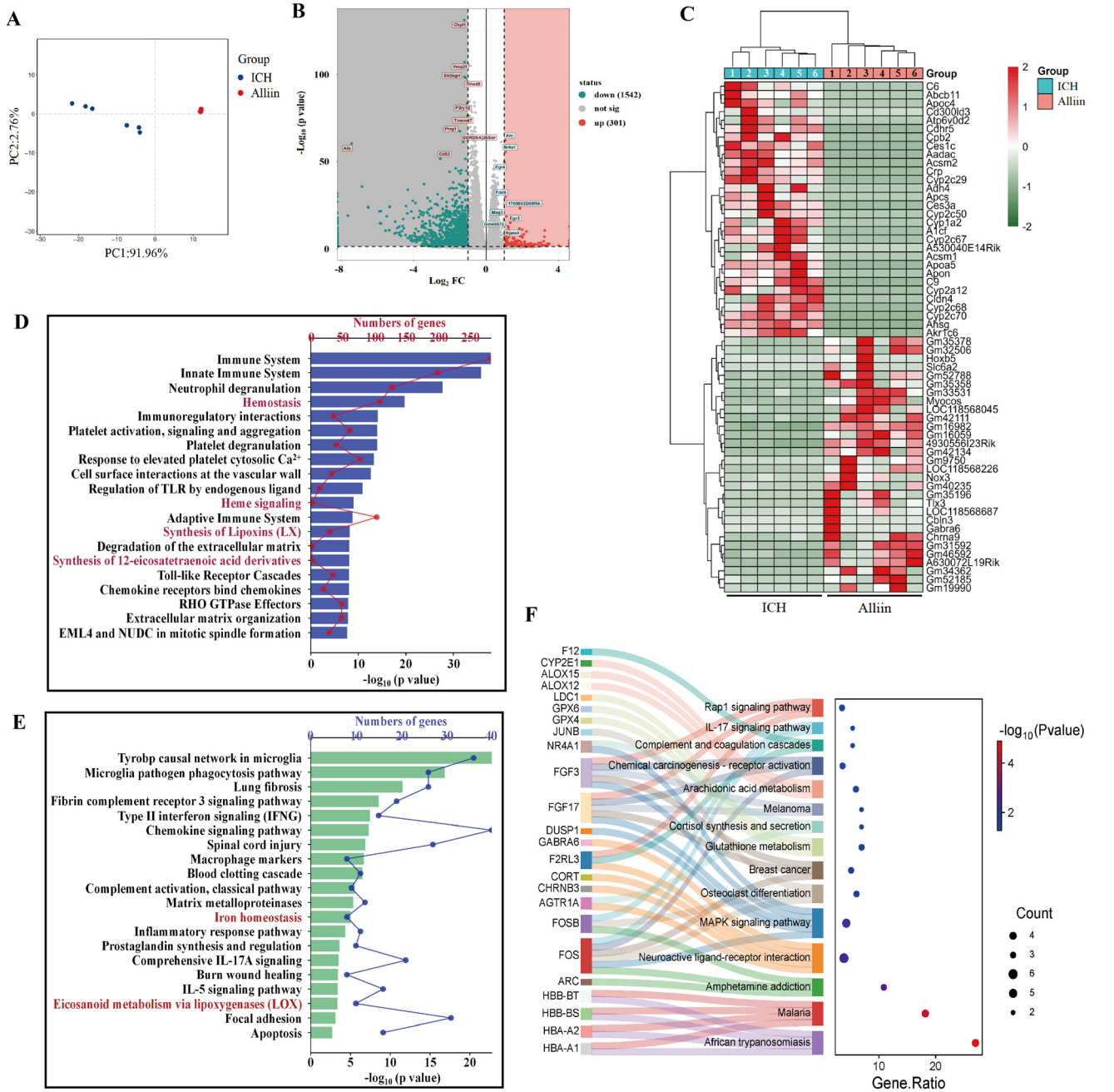

Fig. 7 Transcriptomic differences in the brain between alliin and ICH group. (A) PCA plot among the two groups. (B) Volcano plots of differential genes in the alliin *vs.* ICH group. (C) Heatmaps of the differential genes. (D) Reactome enrichment of the top 20 pathways. (E) WikiPathways enrichment of the top 20 pathways. (F) KEGG enrichment of the top 20 pathways.

3.11. The protective effect of alliin on brain injury in ICH

The examination of alliin's molecular structure through SwissADME assessment revealed its limited capacity to cross the BBB (Fig. 8A). Studies conducted on animal models of collagenase-induced intracerebral hemorrhage (Fig. 8B). Significant weight loss was recorded three days after ICH induction. After treatment with alliin, the weight of the mice gradually recovered (Fig. 8C). Following ICH surgery in mice, the time taken for forelimb placement was notably decreased. Subsequent treatment with alliin increased significantly in forelimb placement time in ICH mice compared to the control group, suggesting that alliin may alleviate hemiplegia symptoms in ICH mice (Fig. 8D). Prior to surgery, all mice had a BMS score of approximately 9. Mice in the control group also scored around 9 for left hind limb motor function. However, ICH group mice exhibited restricted movement in the left hind limb shortly after injury, with a BMS score dropping to

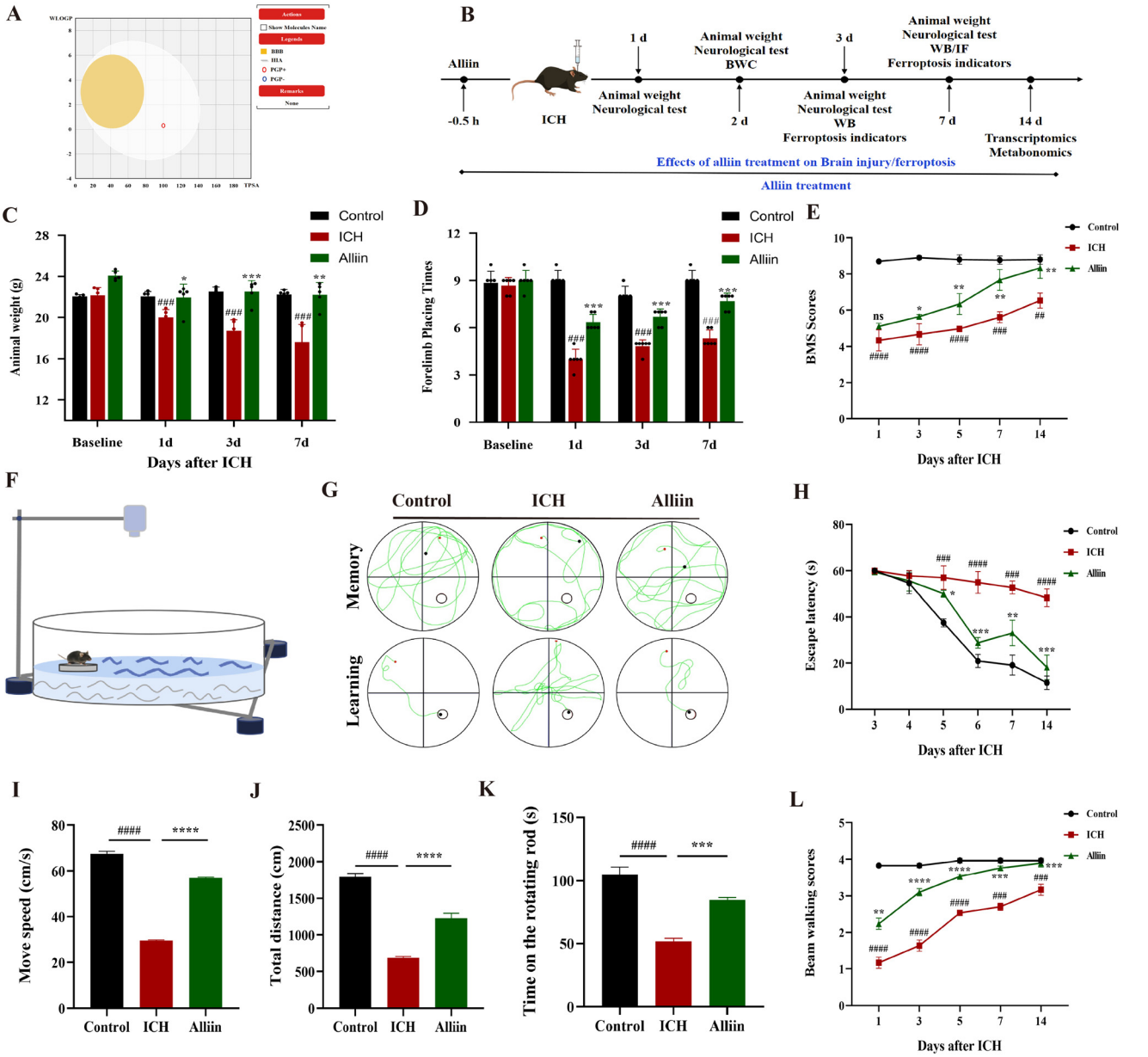

Fig. 8 Effect of alliin in ICH model mice. (A) BOILED-Egg plot. (B) The animal experimental flowchart. (C) Animal body weight evaluated at 1 d, 3 d, and 7 d after ICH, n = 5. (D) Forelimb placing test at 1 d, 3 d, and 7 d after ICH. (E) BMS sore at 1 d, 3 d, 5 d, 7 d and 14 d after ICH. (F–J) Spatial learning and memory were assessed by Morris water maze test, depressive-like behaviors were tested by open field test. (K) The rotating rod test of the mice. (L) Beam walking score of the mice. n = 6 in each group, # compared with control group, *compared with erastin group, *compared with erastin group, $^{*/\#}P < 0.05$, $^{**/\#\#}P < 0.01$, $^{***/\#\#\#}P < 0.001$, $^{****/\#\#\#\#}P < 0.0001$, "ns" means no significant difference ($P > 0.05$).

approximately 4. From the fifth day post-surgery, the BMS scores gradually improved. Throughout the 1st, 3rd, 5th, 7th, and 14th days following surgery, the left hind limb scores of ICH group mice remained significantly lower than those of the control group. After alliin treatment, the BMS score increased from around 5 to near baseline levels (Fig. 8E).

The water maze experiment revealed a notable rise in escape latency among ICH mice in their pursuit of platforms, in contrast to the control group. However, treatment with alliin exhibited the ability to reverse this phenomenon, as evidenced by a decrease in escape latency from day 6 to day 14 when compared to the ICH group (Fig. 8F–J). The rotarod test was used to assess the coordination and balance abilities of the mice. The results showed that mice in the ICH group fell off the rotating rod more quickly, with shorter stay times and at lower rotation speeds. After alliin treatment, the mice's time on the rotating rod significantly increased, and the rotation speed was higher. This indicates that alliin can restore motor coordination and balance abilities in mice after ICH (Fig. 8K). The balance beam test further evaluated the animals'

balance and motor coordination. Post-ICH, mice displayed poor balance and motor coordination; however, these abilities gradually improved in the alliin-treated group (Fig. 8L). These findings were reinforced by neurological function testing, corresponding to the acute and subacute phases of ICH,[26] during which ferroptosis genes reached their peak expression.[17]

Alliin demonstrated a protective effect against brain injury in a mouse model of ICH (Fig. 9A). The effectiveness of alliin in reducing hematoma volume was evaluated through brain

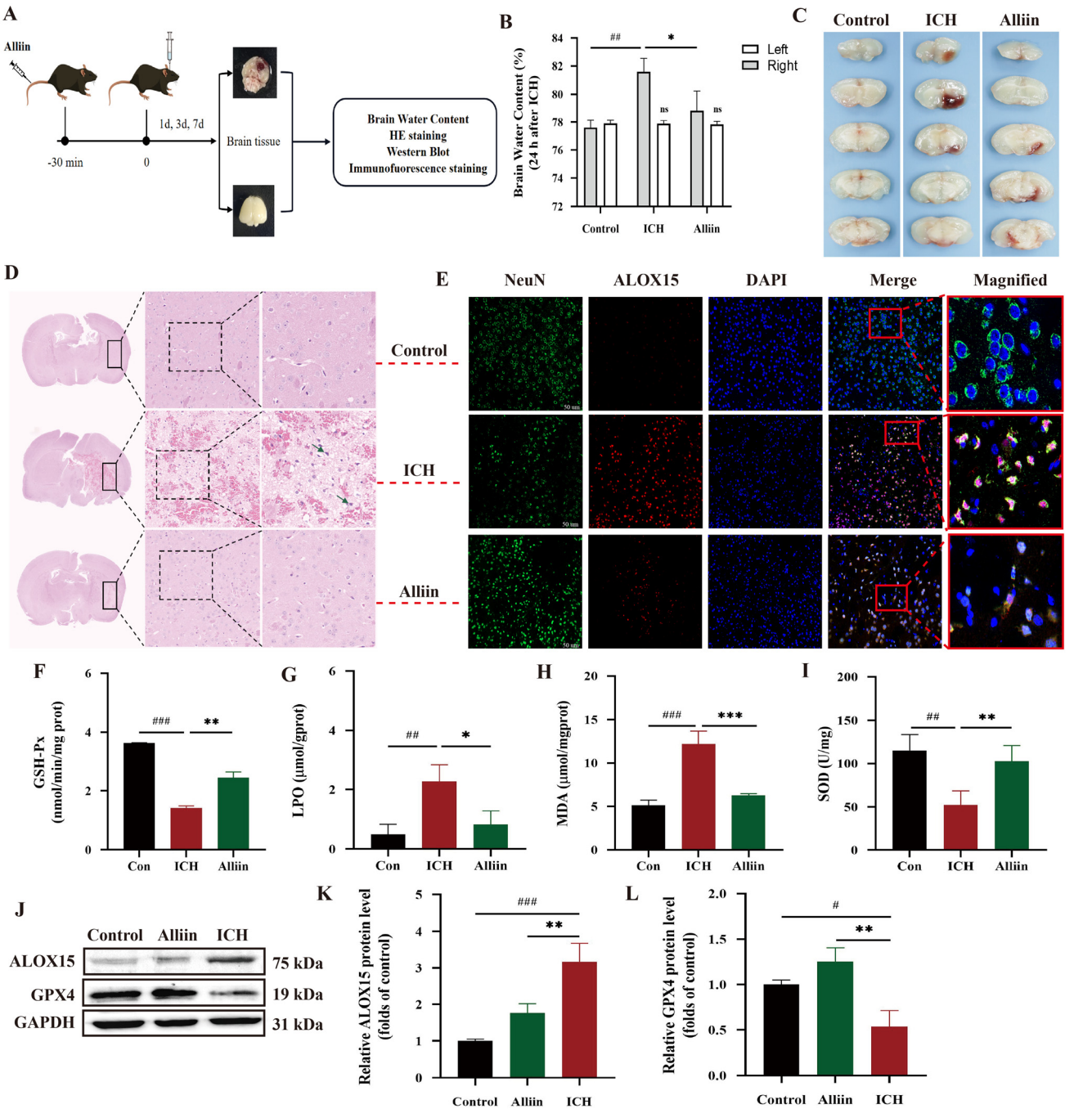

Fig. 9 Effect of alliin in ICH model mice. (A) The animal experimental flowchart. (B) Quantification of brain water content in the left and right brain at 24 h after ICH. (C) Representative pictures of the hemorrhagic lesion in the mice of different groups. (D) Representative images of HE staining of brain slices in the mice of different groups. (E) Spatial expression, and cellular localization of ALOX15 after ICH. Bar 0.5cm. (F–I) GSH-Px, LPO, MDA and SOD contents measured by respective commercial kits at 3 d after ICH (n = 6 in each group). (J–L) The expression of ALOX15 and GPX4 in the mice model (n = 3 in each group). #compared with control group, *compared with erastin group, $^{*/\#}P < 0.05$, $^{**/\#\#}P < 0.01$, $^{***/\#\#\#}P < 0.001$, $^{****/\#\#\#\#}P < 0.0001$, "ns" means no significant difference ($P > 0.05$).

slice imaging. Alliin attenuates neurological deficits and reduces brain edema in ICH mice (Fig. 9B). As illustrated in Fig. 9C, pathological examination revealed substantial hematoma in the ICH group. In contrast, alliin significantly reduced the hematoma volume following ICH injury. HE staining showed irregular neuronal arrangement, vacuolar degeneration, and karyopyknosis in the ICH. Conversely, the administration of alliin notably counteracted this effect (Fig. 9D). The results of immunofluorescence staining indicated a significant reduction in the colocalization of ALOX15 with neuron cells following treatment with alliin compared to treatment with the control alone in the ICH group (Fig. 9E). Additionally, the activity of glutathione peroxidase GSH-Px was notably diminished three days after ICH, but was significantly restored by daily administration of 50 mg kg^{-1} alliin (Fig. 9F). Our study revealed that alliin treatment resulted in a reduction of LPO levels in the brains of ICH mice (Fig. 9G). Following the induction of ICH, there was a significant increase in MDA levels in the ipsilateral hemisphere. Administration of 50 mg kg^{-1} alliin effectively mitigated the ICH-induced elevation of MDA, meanwhile the levels of SOD was increased (Fig. 9H and I).

Data obtained from western blot analysis suggests that the elevated levels of ALOX15 following ICH can be effectively attenuated through treatment with alliin (Fig. 9J–L). Our findings indicate an upregulation of GPX4 expression following treatment with alliin.

3.12. Alliin affects ferroptosis through ALOX15 and GPX4 expression in ICH mice

The susceptibility of phospholipids in brain tissue to peroxidation damage is well-documented. Recent evidence suggests that ferroptosis may contribute significantly to secondary injury in ICH, leading to a growing interest in the potential use of ferroptosis inhibitors in ICH therapy. Our study aimed to investigate the effects and mechanisms of alliin on ferroptosis induced by ICH injury, both in laboratory cell cultures and in live animal models. Our results indicate that alliin effectively inhibits ferroptosis in HT22 cells treated with erastin, and also demonstrates anti-ferroptosis properties in neurons. Subsequent research has shown that alliin effectively improved motor function deficits and reduced cerebral damage by inhibiting ferroptosis in a murine model of ICH. The therapeutic effect of alliin on lipid peroxidation inhibition during ferroptosis may be attributed to the downregulation of ALOX15 expression, which in turn inhibits the oxidation of fatty acids, the formation of lipid peroxides, and the synthesis of AA (Fig. 10). These findings provide convincing evidence for the potential efficacy of alliin as a drug for ICH.

4. Discussion

Our results demonstrate that alliin protects against ferroptosis both *in vitro* and *in vivo* by targeting the ALOX15 pathway. Moreover, our findings indicate that, compared to the ferroptosis inhibitor Fer-1, alliin exhibits significantly better therapeutic effects at a concentration of 400 μM. Additionally, as a naturally derived active small molecule, alliin has relatively lower toxicity compared to synthetic inhibitors. The fatty acid dioxygenase arachidonate 15-lipoxygenase (ALOX15) contains iron and is non-heme. ALOX15 possesses the capability to metabolize varifanyious polyunsaturated fatty acids (PUFAs), yielding biologically active lipid mediators.[27] AA (arachidonic

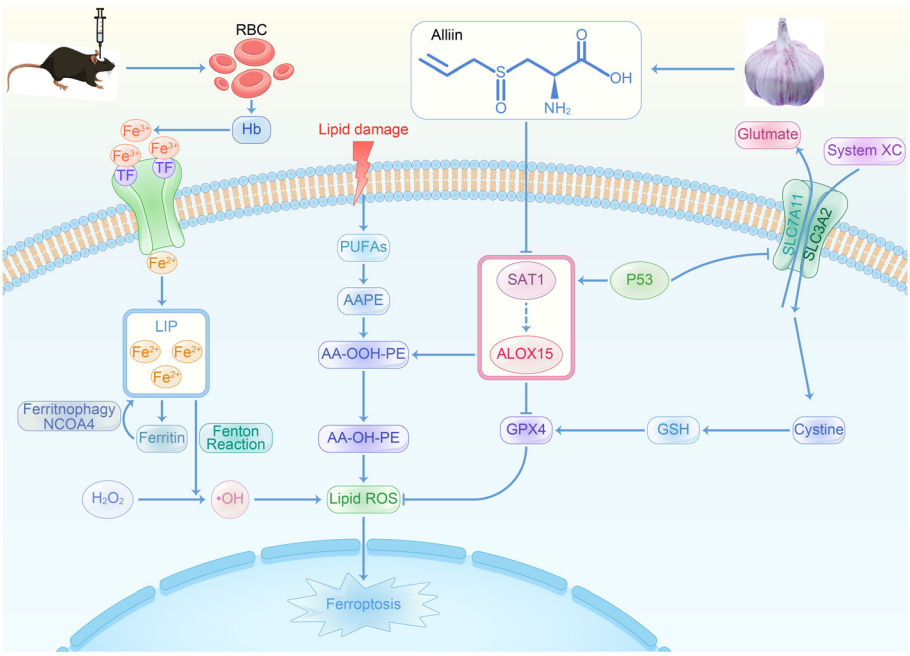

Fig. 10 Proposed mechanistic model of alliin protects against ferroptosis in ICH.

acid) directly oxidizes ferroptotic signals, as evidenced by multiple studies and adrenoyl-phosphatidylethanolamines (AdA-PE) by ALOX15.[28] Serving as a lipoxygenase, ALOX15 plays a pivotal role in driving ferroptosis by regulating lipid peroxidation.[29] The production of OOH-PE metabolites by ALOX15 and their subsequent conversion into hydroxy (OH)-metabolites by GPX4 are essential factors in the determination of cell survival or susceptibility to ferroptosis.[30]

Analysis of differential metabolites in brain tissue after ICH revealed that certain lipids, such as PC, PE, and DG, were significantly upregulated. PC (Phosphatidylcholine) and PE (Phosphatidylethanolamine) are phospholipids and major components of the cell membrane. They are associated with pathways such as linoleic acid metabolism, alpha-linolenic acid metabolism, glycerophospholipid metabolism, and arachidonic acid metabolism. In ferroptosis, polyunsaturated fatty acids (PUFAs) in phosphatidylcholine, such as arachidonic acid, are easily oxidized, generating lipid peroxides. The accumulation of these peroxides leads to the disruption of cell membrane structure, ultimately triggering cell death. The oxidation of phosphatidylcholine is one of the key steps in ferroptosis. Similarly, polyunsaturated fatty acids in phosphatidylethanolamine, such as AA and adrenic acid, are also prone to oxidation during ferroptosis. Studies have shown that phosphatidylethanolamine is one of the primary sources of lipid peroxides.[31] The key enzyme in ferroptosis, ALOX15 (15-lipoxygenase), catalyzes the oxidation of phosphatidylethanolamine, generating lipid peroxides and thereby triggering ferroptosis. DG (Diacylglycerol) is a neutral lipid and an intermediate metabolite of triglycerides and phospholipids. In ferroptosis, diacylglycerol may indirectly participate in the regulation of ferroptosis by influencing lipid metabolism and signal transduction. The accumulation of diacylglycerol may alter the fluidity of the cell membrane and promote the generation of lipid peroxides. In summary, PC and PE are the main sources of lipid peroxides in ferroptosis, and their oxidation is a core mechanism of ferroptosis. DG indirectly participates in the regulation of ferroptosis by affecting lipid metabolism and signal transduction.[32,33]

AA can contribute to lipid peroxidation in the high ROS tumor environment, leading to a decrease in GSH levels, which serves as a marker of ferroptosis.[34] By downregulating ALOX15 expression, alliin reduces lipid peroxidation, thus protecting cells from ferroptotic cell death. Additionally, alliin upregulates GPX4 expression, enhancing cellular antioxidant defense. GPX4, in conjunction with GSH, plays a crucial role in the conversion of hydrogen peroxide and organic hydroperoxides into water or their corresponding alcohols, thereby serving as a crucial defense mechanism against ferroptosis.[35] The metabolites of AA undergo further conversion into leukotriene A4 (LTA4) and lipoxins (LXs) through the enzymatic actions of the 5-lipoxygenase activator protein (5-FLAP) and dehydrase.[36] The primary roles of the 12-LOX and 15-LOX pathways include the biosynthesis of hydroxyeicosatetraenoic acids (HETEs) and LXs.[37,38] In mammalian cells, two isoforms, ALOX15 and ALOX15B, are present. Encoded by the ALOX15, ALOX15 (12/15-LOX) catalyzes the conversion of AA into LXA4, LXB4, and 15-oxo-ETEs. Conversely, ALOX15B metabolizes AA into 15-oxo-ETE and 8SHETE.[38] Oxo ETE is a biologically active medium generated through the oxidation of HETE,[36] with 12(*S*)-hydroxyicosatetraenoic acid (12(*S*)-HETE) and 15(*S*)-hydroxyicosatetraenoic acid (15(*S*)-HETE) identified as primary metabolites produced by the catalysis of arachidonic acid by ALOX15, play critical roles in both physiological and pathological processes.[39] Our results suggest that alliin inhibits the occurrence of ferroptosis by regulating AA metabolism.

Ferroptosis is an iron-dependent form of cell death driven by the excessive peroxidation of polyunsaturated fatty acids (PUFAs) within cellular membranes.[40] During ferroptosis, due to increased iron uptake or decreased iron storage, cells take up transferrin-bound Fe^{3+} *via* transferrin receptor 1 (TFR1)-mediated endocytosis, forming a transferrin-iron complex that enters lysosomes. Subsequently, Fe^{3+} is reduced to Fe^{2+} in lysosomes by ferrireductases or reducing systems such as glutathione (GSH), leading to a significant increase in intracellular free Fe^{2+} levels, which then enter the labile iron pool (LIP). These Fe^{2+} ions catalyze the Fenton reaction ($Fe^{2+} + H_2O_2 \rightarrow Fe^{3+} + {}^{\bullet}OH + OH^-$), converting hydrogen peroxide into highly reactive hydroxyl radicals ($^{\bullet}OH$) and triggering a chain reaction of lipid peroxidation. This results in an explosive accumulation of reactive oxygen species (ROS). When ROS levels exceed the antioxidant defense capacity mediated by GPX4, the radicals attack polyunsaturated fatty acids (PUFAs) in the cell membrane, generating irreversible lipid peroxides (*e.g.*, LOOH). Ultimately, this leads to the disruption of membrane integrity, a dramatic increase in oxidative stress, and the induction of iron-dependent cell death.[41] Mitochondria, which are particularly abundant in PUFAs, rely on these fatty acids to maintain the optimal function of membrane enzymes and transporters, as well as to regulate processes like mitophagy and apoptosis.[42] Ferroptosis, characterized by iron accumulation and lipid peroxidation, has gained attention as a non-apoptotic cell death pathway in recent years.[43,44] PUFAs, containing between 18 and 22 carbon atoms and two or more double bonds, are prone to oxidation by reactive oxygen species, leading to the generation of lipid ROS.[45] Omega-6 and omega-3 are two series of PUFAs. Typical omega-6 fatty acids include AA (C20:4). In addition to ROS and lipoxygenases, such as ALOX15, lipid peroxidation can be triggered.[46] In addition to acting as a reaction substrate for ferroptosis, AA is one of the primary targets of lipoxygenases (LOXs).[47]

Iron in the brain is absorbed by brain cells, with the remaining iron being transported through the BBB. Transferrin and transferrin receptor system (Tf-TfR) are the main mechanisms for transporting iron across the BBB.[48] Our research suggests that the occurrence of ferroptosis after ICH. Under normal physiological conditions, including cellular stress and non-enzymatic autoxidation, lipids are continually peroxidized after ICH.[49] Disruptions in iron levels within the blood and tissues contribute to imbalances in iron metabolism, ultimately generating harmful reactive oxygen species (ROS) and promoting lipid peroxidation, which can be fatal.[50]

Our study indicated that when ICH occurs, the release of Fe^{3+} affects the homeostasis of iron ions, resulted neuronal cells ferroptosis. Divalent iron has the capacity to produce an abundance of ROS through the Fenton reaction, augment ester oxygenase activity, facilitate the oxidation of prevalent unsaturated fatty acids in the cellular membrane, provoke lipid peroxidation, and ultimately result in cellular demise.[44] Excessive iron induces significant ROS generation primarily through the Fenton reaction, leading to inflammation and neuronal death, potentially causing prolonged cognitive deficits and premature cerebral edema.[51,52] Additionally, the metabolism of arachidonic acid is upregulated, increasing the expression of ALOX15 and promoting fatty acid oxidation. This process leads to the formation and accumulation of lipid peroxides, exacerbating damage to neuronal cells.

A thorough examination of the enrichment pathways within three databases revealed that ferroptosis is implicated in neuronal cell following ICH, with lipid peroxidation and LOXs synthesis being key signaling pathways associated with this process. AA, a crucial PUFA, serves as a primary precursor for eicosanoids, specifically a derivative of 12-eicosatetraenoic acid. These molecules, in addition to their participation in numerous physiological functions, are implicated in a variety of pathological conditions such as atherosclerosis, diabetes, and neurological disorders.[53] AA is a prominent constituent within cell membrane lipids, undergoes primary metabolism through three enzyme types: cyclooxygenase (COX), LOX, and cytochrome P450 (CYP450) enzymes. This process results in the production of prostaglandins, hydroperoxyeicosatetraenoic acids, and epoxyeicosatrienoic acids, respectively.[54] The metabolites derived from arachidonic acid collectively referred to as eicosanoids play a crucial role as autocrine and paracrine bioactive mediators, with significant involvement in various physiological and pathological processes.[55] LOXs are enzymes that catalyze the conversion of arachidonic acid into leukotrienes (LTs) and lipoxins (LXs), primarily oxidizing the molecule at positions 5, 12, and 15.[28] Previous research has demonstrated that upregulation of LOX-5, LOX-12, and LOX-15 can increase cellular susceptibility to ferroptosis.[56] Transcriptomics analysis provides support for our hypothesis, indicating that Alliin has the potential to modulate the synthesis of LOXs (such as ALOX15), impacting AA metabolism and the production of eicosanoids and 12-eicosatetraenoic acid derivatives. This cascade of events influences the generation of lipid peroxides and GSH metabolism, while simultaneously maintaining intracellular iron homeostasis. Furthermore, alliin can inhibit the formation of ALOX15 through arachidonic acid metabolism, suppress the production of lipid peroxides, and thereby inhibit the occurrence of ferroptosis, exerting neuroprotective effects against ICH.

Ferroptosis plays a critical role in ischemia/reperfusion (I/R) injury, exacerbating tissue damage through iron accumulation, lipid peroxidation, and the collapse of the antioxidant defense system.[57] Since ALOX15 and its metabolite 15-HpETE are intermediate products generated from the metabolism of arachidonic acid by ALOX15, they directly trigger cellular ferroptosis. ALOX15 is upregulated during I/R, catalyzing the generation of lipid peroxides, and plays a critical role in ferroptosis during I/R injury. In neurodegenerative diseases, iron accumulation in the brain is a common pathological feature. Iron generates reactive oxygen species (ROS) through the Fenton reaction, further exacerbating lipid peroxidation and cellular damage.[58] The increased activity of ALOX15 is closely associated with neuronal death in Alzheimer's disease (AD) and Parkinson's disease (PD). Inhibiting ALOX15 can reduce the generation of lipid peroxides, thereby protecting neurons from ferroptosis-induced damage. In AD and PD, the downregulation or functional loss of GPX4 leads to the accumulation of lipid peroxides, triggering neuronal ferroptosis.[59] ALOX15 promotes the generation of lipid peroxides, while GPX4 inhibits ferroptosis by clearing these peroxides. The balance between the two determines whether neurons undergo ferroptosis. In AD and PD, the upregulation of ALOX15 and downregulation of GPX4 jointly promote the occurrence of ferroptosis. By inhibiting ALOX15 or enhancing GPX4 activity, ferroptosis can be effectively suppressed, thereby protecting neurons. Therefore, alliin, as a natural inhibitor of ALOX15, holds significant clinical potential, particularly in the treatment of myocardial I/R injury and other ferroptosis-related diseases.

5. Conclusion

These findings collectively suggest that ferroptosis plays a crucial role in the pathogenesis of ICH. This study focused on predicting the neuroprotective effect and mechanisms of alliin using transcriptomics, metabolomics, network pharmacology and molecular docking. The findings from both *in vivo* and *in vitro* studies suggest that alliin attenuates neuronal injury by inhibiting ALOX15-dependent ferroptosis, plays a neuroprotective effect on ICH. Alliin holds promise as a therapeutic approach for the prevention and treatment of ICH, indicating its potential as an effective preventive and treatment modality for this condition. The mechanisms of action of alliin is to inhibit the development of ferroptosis in ICH. Nevertheless, this study contains some limitations, additional experimental verification is needed to validate alliin's mechanism of action in treating ICH. Alliin's unique properties – including its natural origin, multi-target effects, and favorable safety profile – suggest broader applications for other ferroptosis-related neurological disorders such as Alzheimer's disease and traumatic brain injury. Key directions for future research will focus on investigating its synergistic effects with existing ICH therapies and validating its therapeutic efficacy in other ferroptosis-related neurological disorders.

Abbreviations

ICH	Intracerebral hemorrhage
BBB	Blood–brain barrier
SBI	Secondary brain injury

LOXs	Lipoxygenases
ALOX15	15-Lipoxygenase
GPX4	Glutathione peroxidase 4
LOOH	Lipid hydroperoxides
SBI	Secondary brain injury
GSH	Glutathione
VOSCs	Volatile organic sulfur-containing compounds
DADS	Diallyl disulfide
DATS	Diallyl trisulfide
RSS	Reactive sulfur species
GSSA	*S*-Allylmercaptoglutathione
MDA	Malondialdehyde
GSH-Px	Glutathione peroxidase
LPO	Lipid peroxidation assay kit
SOD	Superoxide dismutase
ZO-1	Zonula occludens-1
GO	Gene ontology
KEGG	Kyoto encyclopedia of genes and genomes
OB	Oral bioavailability
BP	Biological processes
CC	Cellular components
MF	Molecular functions
PUFAs	Polyunsaturated fatty acids
LTA4	Leukotriene A4
LXs	Lipoxins
5-FLAP	5-Lipoxygenase activator protein
12(*S*)-HETE	12(*S*)-Hydroxyicosatetraenoic acid
15(*S*)-HETE	15(*S*)-Hydroxyicosatetraenoic acid
HETEs	Hydroxyeicosatetraenoic acids
PC	Phosphatidylcholine
PE	Phosphatidyl ethanolamine
DG	Diacylglycerol
MMP	Mitochondrial membrane potential
PCA	Principal component analysis
COX	Cyclooxygenase
CYP450	Cytochrome P450
AA	Arachidonic acid
ROS	Reactive oxygen species
PLOOH	Phospholipid hydroperoxides
TEM	Transmission electron microscopy

Author contributions

Junjun Meng: writing – original draft, conceptualization, investigation, formal analysis, data curation. Chengquan Wen: methodology, investigation, formal analysis. Yang Lu: investigation, formal analysis. Xiaofan Fan: investigation, formal analysis, data curation. Ruili Dang: methodology, investigation, formal analysis. Jianfeng Chu: methodology, investigation, data curation. Pei Jiang: writing – review & editing, supervision, project administration, conceptualization. Wenxiu Han: writing – review & editing, project administration. Lei Feng: writing – review & editing, project administration.

Ethics approval

This study was approved by the Ethics Committee of Jining NO.1 people's hospital (protocol number: JNRM2023DW009).

Data availability

The data used to support the findings of this study are available from the corresponding author upon reasonable request.

Conflicts of interest

We confirm that all co-authors have no known competing financial interests or personal relationships that could have appeared to influence the work reported in this paper.

Acknowledgements

This work was supported by the National Natural Science Foundation of China (82204032), the China Postdoctoral Science Foundation (2023M741365), the Shandong Provincial Natural Science Foundation (ZR2023QH273, ZR2022MH007), the Key R&D Program of Jining (2022YXNS117, 2023YXNS003), the PhD Research Fund of Jining NO.1 People's Hospital (No. 2022-BS-006). And the authors express our gratitude to the China International Medical Foundation Cerebrovascular Disease Youth Innovation Fund (Z-2016-20-2201-11) for its support.

References

1 A. Rauf, T. Abu-Izneid, M. Thiruvengadam, M. Imran, A. Olatunde, M. A. Shariati, S. Bawazeer, S. Naz, S. Shirooie, A. Sanches-Silva, U. Farooq and G. Kazhybayeva, Garlic (Allium sativum L.): Its Chemistry, Nutritional Composition, Toxicity, and Anticancer Properties, *Curr. Top. Med. Chem.*, 2022, **22**, 957–972.

2 E. M. Hegazy, A. Sabry and W. K. B. Khalil, Neuroprotective effects of onion and garlic root extracts against Alzheimer's disease in rats: antimicrobial, histopathological, and molecular studies, *BioTechnologia*, 2022, **103**, 153–167.

3 S. G. Liu, P. Y. Ren, G. Y. Wang, S. X. Yao and X. J. He, Allicin protects spinal cord neurons from glutamate-induced oxidative stress through regulating the heat shock protein 70/inducible nitric oxide synthase pathway, *Food Funct.*, 2015, **6**, 321–330.

4 M. Bigham, A. Mohammadipour, M. Hosseini, A. M. Malvandi and A. Ebrahimzadeh-Bideskan, Neuroprotective effects of garlic extract on dopaminergic neurons of substantia nigra in a rat model of Parkinson's disease: motor and non-motor outcomes, *Metab. Brain Dis.*, 2021, **36**, 927–937.

5 B. Zhai, C. Zhang, Y. Sheng, C. Zhao, X. He, W. Xu, K. Huang and Y. Luo, Hypoglycemic and hypolipidemic effect of S-allyl-cysteine sulfoxide (alliin) in DIO mice, *Sci. Rep.*, 2018, **8**, 3527–3534.
6 A. Ahmad, S.-S. Shin, J.-H. Song, B. Hwang, D.-H. Noh, S. L. Park, W. T. Kim, S.-S. Park, W.-J. Kim and S.-K. Moon, HSPA6 augments garlic extract-induced inhibition of proliferation, migration, and invasion of bladder cancer EJ cells; Implication for cell cycle dysregulation, signaling pathway alteration, and transcription factor-associated MMP-9 regulation, *PLoS One*, 2017, **12**, e0171860.
7 J. W. Zhu, T. Chen, J. Guan, W. B. Liu and J. Liu, Neuroprotective effects of allicin on spinal cord ischemia-reperfusion injury via improvement of mitochondrial function in rabbits, *Neurochem. Int.*, 2012, **61**, 640–648.
8 J.J Lin, T. Chang, W.K Cai, Z. Zhang, Y.X Yang, C. Sun, Z. Y. Li and W. X. Li, Post-injury administration of allicin attenuates ischemic brain injury through sphingosine kinase 2: In vivo and in vitro studies, *Neurochem. Int.*, 2015, **89**, 92–100.
9 B. Ray, N. B. Chauhan and D. K. Lahiri, Oxidative insults to neurons and synapse are prevented by aged garlic extract and S-allyl-L-cysteine treatment in the neuronal culture and APP-Tg mouse model, *J. Neurochem.*, 2011, **117**, 388–402.
10 D. Liang, A. M. Minikes and X. Jiang, Ferroptosis at the intersection of lipid metabolism and cellular signaling, *Mol. Cell*, 2022, **82**, 2215–2227.
11 N. F. Sari, P. Ray, C. Rymer, K. E. Kliem and S. Stergiadis, Garlic and Its Bioactive Compounds: Implications for Methane Emissions and Ruminant Nutrition, *Animals*, 2022, **12**, 2998.
12 Y.-J. He, X.-Y. Liu, L. Xing, X. Wan, X. Chang and H.-L. Jiang, Fenton reaction-independent ferroptosis therapy via glutathione and iron redox couple sequentially triggered lipid peroxide generator, *Biomaterials*, 2020, **241**, 119911.
13 X.-Y. Mao, H.-H. Zhou and W.-L. Jin, Ferroptosis Induction in Pentylenetetrazole Kindling and Pilocarpine-Induced Epileptic Seizures in Mice, *Front. Neurosci.*, 2019, **13**, 721.
14 A. Daina, O. Michielin and V. Zoete, SwissADME: a free web tool to evaluate pharmacokinetics, drug-likeness and medicinal chemistry friendliness of small molecules, *Sci. Rep.*, 2017, **7**, 42717.
15 Y. Atef, K. Kinoshita, Y. Ichihara, K. Ushida, Y. Hirata, Y. Kurauchi, T. Seki and H. Katsuki, Therapeutic effect of allicin in a mouse model of intracerebral hemorrhage, *J. Pharmacol. Sci.*, 2023, **153**, 208–214.
16 A. Yoshimizu, K. Kinoshita, Y. Ichihara, Y. Kurauchi, T. Seki and H. Katsuki, Hydroxychloroquine improves motor function and affords neuroprotection without inhibition of inflammation and autophagy in mice after intracerebral hemorrhage, *J. Neuroimmunol.*, 2022, **362**, 577786.
17 S. Gao, L. Zhou, J. Lu, Y. Fang, H. Wu, W. Xu, Y. Pan, J. Wang, X. Wang, J. Zhang and A. Shao, Cepharanthine Attenuates Early Brain Injury after Subarachnoid Hemorrhage in Mice via Inhibiting 15-Lipoxygenase-1-Mediated Microglia and Endothelial Cell Ferroptosis, *Oxid. Med. Cell. Longevity*, 2022, **2022**, 4295208.
18 M. S. Nadeem, I. Kazmi, I. Ullah, K. Muhammad and F. Anwar, Allicin, an Antioxidant and Neuroprotective Agent, Ameliorates Cognitive Impairment, *Antioxidants*, 2021, **11**, 87.
19 B. Yudhistira, F. Punthi, J. A. Lin, A. S. Sulaimana, C. K. Chang and C. W. Hsieh, S-Allyl cysteine in garlic (Allium sativum): Formation, biofunction, and resistance to food processing for value-added product development, *Compr. Rev. Food Sci. Food Saf.*, 2022, **21**, 2665–2687.
20 Y. Liu, P. Zhu, Y. Wang, Z. Wei, L. Tao, Z. Zhu, X. Sheng, S. Wang, J. Ruan, Z. Liu, Y. Cao, Y. Shan, L. Sun, A. Wang, W. Chen and Y. Lu, Antimetastatic Therapies of the Polysulfide Diallyl Trisulfide against Triple-Negative Breast Cancer (TNBC) via Suppressing MMP2/9 by Blocking NF-kappaB and ERK/MAPK Signaling Pathways., *PLoS One*, 2015, **10**, 0123781–0123799.
21 R. Natarajan and J. L. Nadler, Lipid inflammatory mediators in diabetic vascular disease, *Arterioscler., Thromb., Vasc. Biol.*, 2004, **24**, 1542–1548.
22 J. Meng, H. Zhong, X. Chu, J. Guo, S. Zhao, T. Shen, W. Sun, J. Wang and P. Jiang, Comparative analysis of chemical elements and metabolites in diverse garlic varieties based on metabolomics and ionomics, *Food Sci. Nutr.*, 2024, **12**, 7719–7736.
23 Y. Zhou, Y. Shen, C. Chen, X. Sui, J. Yang, L. Wang and J. Zhou, The crosstalk between autophagy and ferroptosis: what can we learn to target drug resistance in cancer?, *Cancer Biol. Med.*, 2019, **16**, 630–646.
24 R. Zhao, Y. Lv, T. Feng, R. Zhang, L. Ge, J. Pan, B. Han, G. Song and L. Wang, ATF6α promotes prostate cancer progression by enhancing PLA2G4A-mediated arachidonic acid metabolism and protecting tumor cells against ferroptosis, *Prostate*, 2022, **82**, 617–629.
25 A. Zare, P. Farzaneh, Z. Pourpak, F. Zahedi, M. Moin, S. Shahabi and Z. M. Hassan, Purified Aged Garlic Extract Modulates Allergic Airway Inflammation in Balb/c Mice, *Iran. J. Allergy, Asthma Immunol.*, 2008, **7**, 133–141.
26 Q. Li, A. Weiland, X. Chen, X. Lan, X. Han, F. Durham, X. Liu, J. Wan, W. C. Ziai, D. F. Hanley and J. Wang, Ultrastructural Characteristics of Neuronal Death and White Matter Injury in Mouse Brain Tissues After Intracerebral Hemorrhage: Coexistence of Ferroptosis, Autophagy, and Necrosis, *Front. Neurol.*, 2018, **9**, 581.
27 H. Kuhn, L. Humeniuk, N. Kozlov, S. Roigas, S. Adel and D. Heydeck, The evolutionary hypothesis of reaction specificity of mammalian ALOX15 orthologs, *Prog. Lipid Res.*, 2018, **72**, 55–74.
28 X. Xu, J. Li, Y. Zhang and L. Zhang, Arachidonic Acid 15-Lipoxygenase: Effects of Its Expression, Metabolites, and Genetic and Epigenetic Variations on Airway Inflammation, *Allergy, Asthma Immunol. Res.*, 2021, **13**, 684.
29 J. Zhao, Y. Wu, S. Liang and X. Piao, Activation of SSAT1/ALOX15 Axis Aggravates Cerebral Ischemia/Reperfusion

Injury via Triggering Neuronal Ferroptosis, *Neuroscience*, 2022, **485**, 78–90.

30 V. E. Kagan, G. Mao, F. Qu, J. P. F. Angeli, S. Doll, C. S. Croix, H. H. Dar, M. Conrad and H. Bayır, Oxidized arachidonic and adrenic PEs navigate cells to ferroptosis, *Nat. Chem. Biol.*, 2017, **13**, 81–90.

31 H.-f. Yan, T. Zou, Q.-z. Tuo, S. Xu, H. Li, A. A. Belaidi and P. Lei, Ferroptosis: mechanisms and links with diseases, *Signal Transduction Targeted Ther.*, 2021, **6**, 49.

32 X. Jiang, B. R. Stockwell and M. Conrad, Ferroptosis: mechanisms, biology and role in disease, *Nat. Rev. Mol. Cell Biol.*, 2021, **22**, 266–282.

33 B. Qiu, F. Zandkarimi, C. T. Bezjian, E. Reznik, R. K. Soni, W. Gu, X. Jiang and B. R. Stockwell, Phospholipids with two polyunsaturated fatty acyl tails promote ferroptosis, *Cell*, 2024, **187**, 1177–1190.e18.

34 M. Gao, J. Deng, F. Liu, A. Fan, Y. Wang, H. Wu, D. Ding, D. Kong, Z. Wang, D. Peer and Y. Zhao, Triggered ferroptotic polymer micelles for reversing multidrug resistance to chemotherapy, *Biomaterials*, 2019, **223**, 119486.

35 K. Aoyama, Glutathione in the Brain, *Int. J. Mol. Sci.*, 2021, **22**, 5010.

36 W. S. Powell and J. Rokach, Biosynthesis, biological effects, and receptors of hydroxyeicosatetraenoic acids (HETEs) and oxoeicosatetraenoic acids (oxo-ETEs) derived from arachidonic acid, *Biochim. Biophys. Acta*, 2015, **1851**, 340–355.

37 B. Porro, P. Songia, I. Squellerio, E. Tremoli and V. Cavalca, Analysis, physiological and clinical significance of 12-HETE: a neglected platelet-derived 12-lipoxygenase product, *J. Chromatogr. B: Anal. Technol. Biomed. Life Sci.*, 2014, **964**, 26–40.

38 A. R. Green, C. Freedman, J. Tena, B. E. Tourdot, B. Liu, M. Holinstat and T. R. Holman, 5 S,15 S-Dihydroperoxyeicosatetraenoic Acid (5,15-diHpETE) as a Lipoxin Intermediate: Reactivity and Kinetics with Human Leukocyte 5-Lipoxygenase, Platelet 12-Lipoxygenase, and Reticulocyte 15-Lipoxygenase-1, *Biochemistry*, 2018, **57**, 6726–6734.

39 M. Colakoglu, S. Tuncer and S. Banerjee, Emerging cellular functions of the lipid metabolizing enzyme 15-Lipoxygenase-1, *Cell Proliferation*, 2018, **51**, e12472.

40 R. Fernandez-Acosta, B. Hassannia, J. Caroen, B. Wiernicki, D. Alvarez-Alminaque, B. Verstraeten, J. Van der Eycken, P. Vandenabeele, T. VandenBerghe and G. L. Pardo-Andreu, Molecular Mechanisms of Nemorosone-Induced Ferroptosis in Cancer Cells, *Cells*, 2023, **12**, 735.

41 M. Zhang, Z. Yan, Z. Chen, H. Ouyang, C. Tan and C. Lu, Ferroptosis in Intracerebral Hemorrhage: A Panoramic Perspective of the Metabolism, Mechanism and Theranostics, *Aging Dis.*, 2022, **13**, 1348.

42 A. Y. Andreyev, H. S. Tsui, G. L. Milne, V. V. Shmanai, A. V. Bekish, M. A. Fomich, M. N. Pham, Y. Nong, A. N. Murphy, C. F. Clarke and M. S. Shchepinov, Isotope-reinforced polyunsaturated fatty acids protect mitochondria from oxidative stress, *Free Radicals Biol. Med.*, 2015, **82**, 63–72.

43 M. Chang, Z. Hou, M. Wang, C. Yang, R. Wang, F. Li, D. Liu, T. Peng, C. Li and J. Lin, Single-Atom Pd Nanozyme for Ferroptosis-Boosted Mild-Temperature Photothermal Therapy, *Angew. Chem., Int. Ed.*, 2021, **60**, 12971–12979.

44 D. Tang, X. Chen, R. Kang and G. Kroemer, Ferroptosis: molecular mechanisms and health implications, *Cell Res.*, 2021, **31**, 107–125.

45 M. J. Kim, G. J. Yun and S. E. Kim, Metabolic Regulation of Ferroptosis in Cancer, *Biology*, 2021, **10**, 83.

46 S. E. Wenzel, Y. Y. Tyurina, J. Zhao, C. M. St. Croix, H. H. Dar, G. Mao, V. A. Tyurin, T. S. Anthonymuthu, A. A. Kapralov, A. A. Amoscato, K. Mikulska-Ruminska, I. H. Shrivastava, E. M. Kenny, Q. Yang, J. C. Rosenbaum, L. J. Sparvero, D. R. Emlet, X. Wen, Y. Minami, F. Qu, S. C. Watkins, T. R. Holman, A. P. VanDemark, J. A. Kellum, I. Bahar, H. Bayır and V. E. Kagan, PEBP1 Wardens Ferroptosis by Enabling Lipoxygenase Generation of Lipid Death Signals, *Cell*, 2017, **171**, 628–641.e26.

47 J. Wen, A. Aili, Y. X. Yan, Y. Lai, S. Niu, S. He, X. Zhang, G. Zhang and J. Li, OIT3 serves as a novel biomarker of hepatocellular carcinoma by mediating ferroptosis via regulating the arachidonic acid metabolism, *Front. Oncol.*, 2022, **12**, 628.

48 C. C. Chiueh, Iron Overload, Oxidative Stress, and, Axonal Dystrophy in Brain Disorders, *Pediatr. Neurol.*, 2001, **25**, 138–147.

49 T. S. Anthonymuthu, Y. Y. Tyurina, W.-Y. Sun, K. Mikulska-Ruminska, I. H. Shrivastava, V. A. Tyurin, F. B. Cinemre, H. H. Dar, A. P. VanDemark, T. R. Holman, Y. Sadovsky, B. R. Stockwell, R.-R. He, I. Bahar, H. Bayır and V. E. Kagan, Resolving the paradox of ferroptotic cell death: Ferrostatin-1 binds to 15LOX/PEBP1 complex, suppresses generation of peroxidized ETE-PE, and protects against ferroptosis, *Redox Biol.*, 2021, **38**, 101744.

50 J. Wan, H. Ren and J. Wang, Iron toxicity, lipid peroxidation and ferroptosis after intracerebral haemorrhage, *Stroke Vasc. Neurol.*, 2019, **4**, 93–95.

51 Q. Bai, J. Liu and G. Wang, Ferroptosis, a Regulated Neuronal Cell Death Type After Intracerebral Hemorrhage, *Front. Cell. Neurosci.*, 2020, **14**, 591874.

52 Y. Zhang, X. Zhang, V. W. Yong and M. Xue, Vildagliptin improves neurological function by inhibiting apoptosis and ferroptosis following intracerebral hemorrhage in mice, *Neurosci. Lett.*, 2022, **776**, 136579.

53 O. Kursun, H. Karatas, H. Bariskaner and S. Ozturk, Arachidonic Acid Metabolites in Neurologic Disorders, *CNS Neurol. Disord.:Drug Targets*, 2022, **21**, 150–159.

54 T. Wang, X. Fu, Q. Chen, J. K. Patra, D. Wang, Z. Wang and Z. Gai, Arachidonic Acid Metabolism and Kidney Inflammation, *Int. J. Mol. Sci.*, 2019, **20**, 3683.

55 A. A. Rand, B. Barnych, C. Morisseau, T. Cajka, K. S. S. Lee, D. Panigrahy and B. D. Hammock, Cyclooxygenase-derived proangiogenic metabolites of epoxyeicosatrienoic acids, *Proc. Natl. Acad. Sci. U. S. A.*, 2017, **114**, 4370–4375.

56 R. Shah, M. S. Shchepinov and D. A. Pratt, Resolving the Role of Lipoxygenases in the Initiation and Execution of Ferroptosis, *ACS Cent. Sci.*, 2018, **4**, 387–396.
57 K.-M. Fang, F.-C. Cheng, Y.-L. Huang, S.-Y. Chung, Z.-Y. Jian and M.-C. Lin, Trace Element, Antioxidant Activity, and Lipid Peroxidation Levels in Brain Cortex of Gerbils After Cerebral Ischemic Injury, *Biol. Trace Elem. Res.*, 2013, **152**, 66–74.
58 A. A. Belaidi and A. I. Bush, Iron neurochemistry in Alzheimer's disease and Parkinson's disease: targets for therapeutics, *J. Neurochem.*, 2016, **139**, 179–197.
59 F. P. Bellinger, M. T. Bellinger, L. A. Seale, A. S. Takemoto, A. V. Raman, T. Miki, A. B. Manning-Boğ, M. J. Berry, L. R. White and G. W. Ross, Glutathione Peroxidase 4 is associated with Neuromelanin in Substantia Nigra and Dystrophic Axons in Putamen of Parkinson's brain, *Mol. Neurodegener.*, 2011, **6**, 8–18.